

Impact of Exchange-Correlation Functionals on Phonon Hydrodynamics: A Study of Fluorides (NaF, LiF) and Alkali Hydrides (LiH, NaH) Under Guyer's Criteria

Jamal Abou Haibeh and Samuel Huberman

Department of Chemical Engineering, McGill University, Montreal, Québec H3A 0C5, Canada

In this study, we examine the effect of various exchange-correlation (XC) functionals, including the Perdew-Burke-Ernzerhof generalized gradient approximation (PBE), the modified Perdew-Burke-Ernzerhof generalized gradient approximation (PBESOL), and the local density approximation (LDA), on the calculations of electrical, mechanical, and thermal properties of sodium fluoride (NaF), lithium fluoride (LiF), lithium hydride (LiH), and sodium hydride (NaH). The lattice thermal conductivity is computed based on an iterative solution of the Boltzmann transport equation (BTE). Guyer's criteria [1] is applied to predict the phonon hydrodynamics regime. Based on our calculations, second sound in NaF can be observed at a temperature of 15 K, in agreement with previous experimental observations from Jackson *et al.* [2]. The impact of isotopes on the calculated lattice thermal conductivity and phonon hydrodynamics windows is also reported. We find that the selection of a functional impacts the prediction of thermal conductivity and the window for observation of phonon hydrodynamics.

I. INTRODUCTION

Density-functional theory (DFT) calculations are powerful tools for modeling complex materials in the fields of materials science, physics, chemistry, and engineering. The growth in the usage of DFT over more than five decades is primarily due its ability to balance accuracy and computational cost [3]. At the heart of this balance lies the exchange-correlation (XC) functional which shoulders the duty of approximating electron interactions that occur in many-body systems. This functional operates on a foundation that facilitates various approximations. To aid this, pseudopotentials streamline the process significantly, replacing the non-trivial influences of core electrons with effective potentials.

The bottom rung in the ladder of functional approximations is the local density approximation (LDA), which approximates the exchange-correlation energy based on a uniform electron gas model [4]. Advancements led to the formulation of generalized gradient approximations (GGA), which extend the LDA approach by incorporating gradient corrections to the electron density, enhancing the accuracy of DFT calculations. Several GGA functions have since been developed since there are multiple ways to characterize the gradient of electron density [4–6]. The most two common GGA functions are the Perdew-Burke-Ernzerhof generalized gradient approximation (PBE) [4] and the modified Perdew-Burke-Ernzerhof generalized gradient approximation (PBESOL) [6]. PBE includes the gradient of the electron density in the exchange-

correlation function and improves upon LDA by capturing some non-local effects, but there remain limitations, particularly for systems with strongly localized electrons (e.g., transition metal complexes [7]).

Given these approximations, deviations between experimental and theoretical predictions are expected. It is well known that the LDA under-predicts the bandgap in silicon by about 50 % [8–10]. However, even with this well-known and significant discrepancy, accurate DFT-based predictions of the thermal conductivity of silicon have been obtained [11–13]. For instance, Jain and McGaughey later showed that the impact of the choice of pseudopotential and XC functional on thermal conductivity predictions can impact accuracy by up to 17% [14].

Going beyond thermal conductivity, recent work has built upon these first principles calculations to investigate phonon hydrodynamics, a regime of thermal transport that lies between the diffusive and ballistic regimes. [15,16]. One of the signatures of phonon hydrodynamics is “second sound,” where temperature propagates as a wave. This phenomenon has been observed in a small number of materials [2,17–21]. One of the early experimental observations of second sound was found in NaF at temperatures of about ~15-20 K [2]. The objective of this work is to examine the impact of the choice of XC functionals (PBE, PBESOL, LDA) on the prediction of phonon hydrodynamics in fluorides (NaF, LiF) and alkali hydrides (LiH, NaH).

II. THEORY

Based on approximate solutions to the phonon Boltzmann Transport Equation, a condition for the existence phonon hydrodynamics was proposed by Guyer and Krumhansl, henceforth referred to as Guyer’s criteria [1]. This condition states that phonon hydrodynamics can be observed if the average boundary scattering rate $\langle \tau_B^{-1} \rangle$ is greater than the average Umklapp scattering rate $\langle \tau_U^{-1} \rangle$ but less than the average Normal scattering rate $\langle \tau_N^{-1} \rangle$ at a given temperature and a characteristic length [1]

$$\langle \tau_N^{-1} \rangle > \langle \tau_B^{-1} \rangle > \langle \tau_U^{-1} \rangle \quad (1)$$

In other words, phonon hydrodynamics can be observed if Normal scattering dominates over Umklapp scattering. The average resistive scattering rate $\langle \tau_R^{-1} \rangle$ (sum of Umklapp and isotope scattering rates) can also be used instead of the average Umklapp scattering rate

$$\langle \tau_N^{-1} \rangle > \langle \tau_B^{-1} \rangle > \langle \tau_R^{-1} \rangle \quad (2)$$

where $\langle \rangle$ represents the average. The average scattering rate $\langle \tau^{-1} \rangle$ is defined as

$$\langle \tau^{-1} \rangle = \frac{\sum \tau_i^{-1} C_i}{\sum C_i} = \frac{\sum \tau_i^{-1} C_i}{C} \quad (3)$$

Where C_i and C are the heat capacity for a given phonon mode and the total heat capacity of all phonon modes, respectively. Other expressions for average scattering rates may be selected, but here we follow previous studies [22]. We employ an *ab-initio* framework to study phonon hydrodynamics in crystal fluorides and alkali hydrides. The details of the DFT calculations can be found in Sec. I of the Supplemental Material.

III. RESULTS

A. Properties of NaF

Lattice constant a (Å), dielectric constant ϵ , Born effective charge Z^* , phonon frequencies at gamma ω (THz), and band gap E_g (eV) of calculated, theoretical data and experimental data from the literature for NaF are shown in Table I. The calculated equilibrium lattice constants from PBE, PBESOL, and LDA functionals are 4.72, 4.65, and 4.52 Å, respectively, well-consistent with the experimental value $a(\text{exp}) = 4.6295$ Å that was measured at 0 °C by Pathak *et al.* [23]. The percentage errors ($|\text{experimental value} - \text{theoretical value}| / \text{theoretical value} \times 100$ %) are 1.92, 0.44, and 2.42 %, respectively. The dielectric-constant tensor ‘ ϵ ’ and Born effective charges ‘ Z^* ’ are calculated based on the density functional perturbation theory (DFPT) to capture the longitudinal and transverse optical phonon (LO-TO) splitting at the gamma point [24]. For fluorides and alkali hydrides (NaF, LiF, LiH, and NaH), the underlying Bravais lattice is cubic (FCC crystal); hence there is only one independent component in the Born effective charge tensor. Our calculations for the Born effective charge using PBE are consistent with the experimental value ($Z^*_{\text{exp}} = 1.02$) [25]. In contrast, we observe that these functionals (PBE, PBESOL, and LDA) are not accurate in computing the electrical band gap. It was previously found that other functionals, such as the modified Becke–Johnson (mBJ) exchange potential, can be used to obtain a more accurate estimate of the band gap [26–28]. The electrical band structures of fluoride and alkali hydride materials can be found in Sec. III of the Supplemental Material, where the Fermi energy (E_f) is shifted to zero eV.

Table I. Lattice constant a (Å), dielectric constant ϵ , Born effective charge Z^* , phonon frequencies at gamma ω (THz), and band gap E_g (eV) of calculated, other theoretical data, and experimental data for NaF.

	PBE	PBESOL	LDA	Other theoretical data	Experiments
a	4.72	4.65	4.52	4.67 ^a , 4.69 ^b , 4.63 ^c , 4.80 ^d , 4.695 ^{e1} , 4.693 ^{e2}	4.6295 ^f , 4.6342 ^g
ϵ	1.86	1.89	1.93	1.85 ^e	1.74 ^h
Z^*	1.02	1.01	0.99	1.019 ^e , 0.956 ⁱ	1.02 ^j
ω_{LO}	11.67	12.01	12.81	11.90 ^e	12.65 ^k
ω_{TO}	6.78	7.24	8.32	6.95 ^e	7.385 ^k
E_g	6.02	6.11	6.34	12.0 ^a , 6.12 ^{e3} , 7.11 ^{e4} , 11.69 ^{e5}	11.50 ^l

^aRef. [29]. ^bRef. [30]. ^cRef. [31]. ^dRef. [32]. ^eRef. [28]. ^{e1}Ref. [28], calculated using full-potential linearized augmented plane wave (FP-LAPW) method. ^{e2}Ref. [28], calculated using pseudopotential. ^{e3}Ref. [28], calculated using generalized gradient approximation (GGA). ^{e4}Ref. [28], calculated using Engel–Vosko (EV) approximation. ^{e5}Ref. [28], calculated using the modified Becke–Johnson (mBJ) exchange potential. ^fRef. [23], measured at 0 °C. ^gRef. [33]. ^hRef. [34]. ⁱRef. [35]. ^jRef. [25]. ^kRef. [36]. ^lRef. [37].

The agreement between the calculated phonon dispersion and experimental data verifies the accuracy of the calculations of the second-order interatomic force constants. The frequencies of the longitudinal and transverse optical phonon (LO-TO) at the gamma point are listed in Table I. The calculated phonon dispersion and phonon density of states are presented in Fig. 1 for NaF. In Fig. 1 (a), we compare the calculated and the measured phonon dispersion relations [38]. While the PBE, PBESOL and LDA phonon dispersions share qualitative agreement with each other, the PBE functionals provides the most reasonable agreement with the measured values [38].

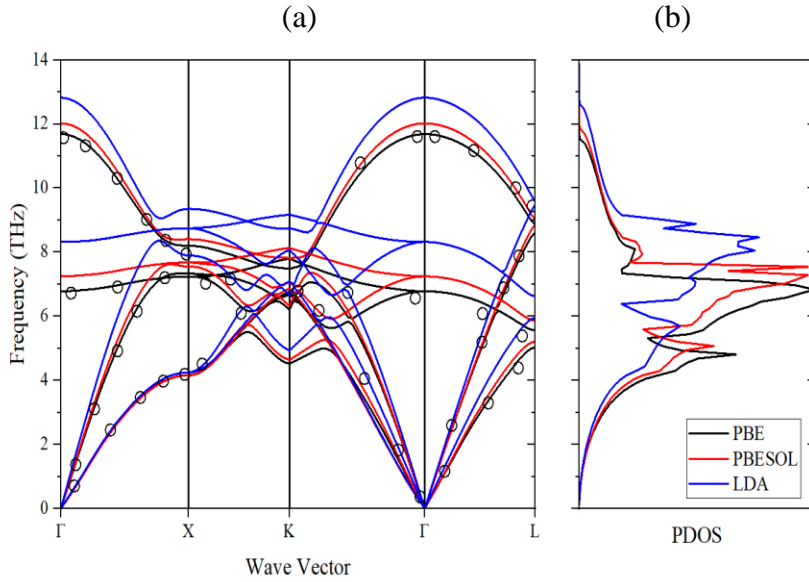


FIG. 1. (a) Calculated phonon dispersion and (b) phonon density of states for NaF. Calculations were done with PBE (black solid lines), PBESOL (red solid lines), and LDA (blue solid lines). Black circles are the measured data from Ref. [38].

The mechanical properties for NaF, including the bulk modulus and elastic constants, are given in Table II. The three independent components of a cubic crystal are C_{11} , C_{12} , and C_{44} . We calculated bulk modulus ‘B’ and elastic constants ‘ C_{ij} ’ at 0 K. Lewis *et al.* measured elastic constants of NaF at 4.2 K [39], which differ slightly from the calculated values at 0 K. Our calculated bulk modulus and elastic constants for NaF do not show that a single functional consistently matches with the experimental results (see LDA for C_{44} and PBE for B for example), but overall agreement is found [39–41].

Table II. Bulk modulus B (GPa) and elastic constants C_{ij} (GPa) of calculated, other theoretical data, and experimental data for NaF.

	PBE	PBESOL	LDA	Other theoretical data	Experiments
B	46.79	48.46	61.14	40.8 ^a , 61.6 ^b	45.7 ^c
C_{11}	95.68	101.86	133.97	97.1 ^d , 145.14 ^e	97.0 ^c , 108.5 ^f , 96.90 ^g
C_{12}	22.84	21.75	24.73	24.3 ^d , 33.83 ^e	24.3 ^c , 22.90 ^f , 24.50 ^g
C_{44}	26.35	26.59	28.31	28.0 ^d , 33.83 ^e	28.1 ^c , 28.99 ^f , 28.01 ^g

^aRef. [32]. ^bRef. [42], calculated using LDA. ^cRef. [41]. ^dRef. [43]. ^eRef. [44]. ^fRef. [39]. ^gRef. [40].

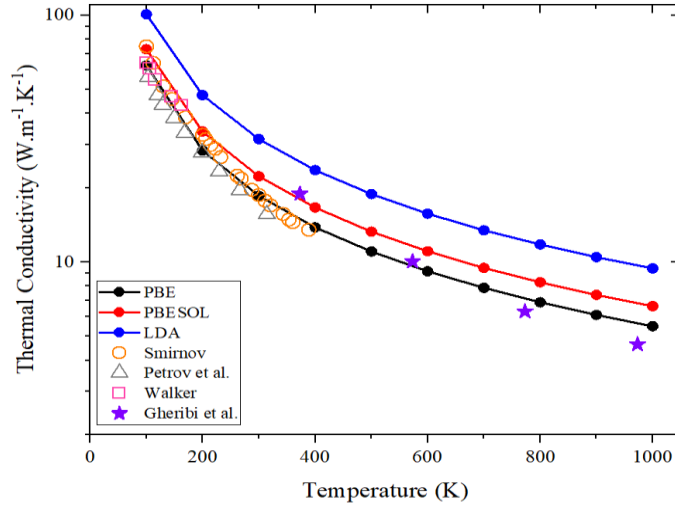


FIG. 2. Calculated lattice thermal conductivity for NaF. Calculations were done with PBE (black circles), PBESOL (red circles), and LDA (blue circles). Experimental data: Ref. [45] (orange circles), Ref. [46] (gray triangles), Ref. [47] (pink squares). Theoretical data: Ref. [48] (purple stars).

The lattice thermal conductivity was calculated for temperatures ranging from 100 K to 1000 K and compared with values from the literature [45–48], as shown in Fig. 2. Experimental values of thermal conductivity were measured below 400 K [45–47]. Most experimental values closely follow the PBE prediction but are systematically offset from the LDA prediction. Table III lists the thermal conductivity, specific heat, average Grüneisen parameter, and density values at room temperature. It was found that PBE yields the smallest percent error (0.86 %) for the theoretical thermal conductivity for NaF at room temperature. All values obtained in Table III using PBE agree well with experimental data [39,41,45,49,50].

Table III. Thermal conductivity k ($\text{W}\cdot\text{m}^{-1}\cdot\text{K}^{-1}$), specific heat c_p ($\text{kJ}\cdot\text{kg}^{-1}\cdot\text{K}^{-1}$), average Grüneisen parameter $\bar{\gamma}$, and density ρ ($\text{g}\cdot\text{cm}^{-3}$) of calculated, other theoretical data, and experimental data for NaF at room temperature.

	PBE	PBESOL	LDA	Other theoretical data	Experiments
k	18.54	22.26	31.48	-	18.7 ^a
c_p	1.09	1.08	1.06	-	1.09 ^b
$\bar{\gamma}$	1.78	1.61	1.59	1.79 ^c	1.83 ^c
ρ	2.66	2.78	3.01	2.80 ^d	2.769 ^e , 2.804 ^f

^aRef. [45]. ^bRef. [49], measured at 276.20 K. ^cRef. [50]. ^dRef. [43]. ^eRef. [39]. ^fRef. [41].

An example of the application of Guyer’s criteria for $L = 8.3$ mm is shown in Fig. 3. The hydrodynamic window is located up to 15.5 K for PBE, up to 16 K for PBESOL, and up to 17.2 K

for LDA, which agrees with the experimental observation of second sound in NaF [2]. These ranges indicate the temperature intervals within which each functional predicts phonon hydrodynamics. For NaF, PBE has the narrowest phonon hydrodynamic temperature range, PBESOL has a slightly broader temperature range, and LDA has the widest temperature range.

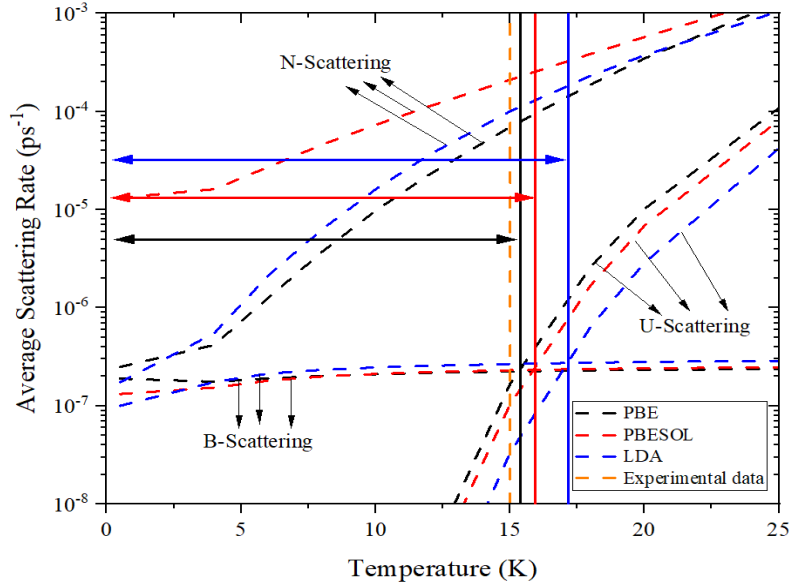


FIG. 3. Phonon hydrodynamics windows for NaF at $L = 8.3$ mm. Calculations were done with PBE (black dashed lines), PBESOL (red dashed lines), and LDA (blue dashed lines). Double arrow lines show the hydrodynamics range for each functional. The experimental value [2] is shown as a dashed vertical orange line.

By applying Guyer's criteria at different temperatures and characteristic lengths, the 'phase space' of phonon transport regimes can be determined. Fig. 4 shows the three phonon thermal transport regimes (ballistic, hydrodynamic, and diffusive) for temperatures up to 80 K and characteristic lengths of $10^2 - 10^8$ nm. The differences between PBE and PBESOL may not be discernible at higher temperatures, but become apparent when compared to LDA or at lower temperatures.

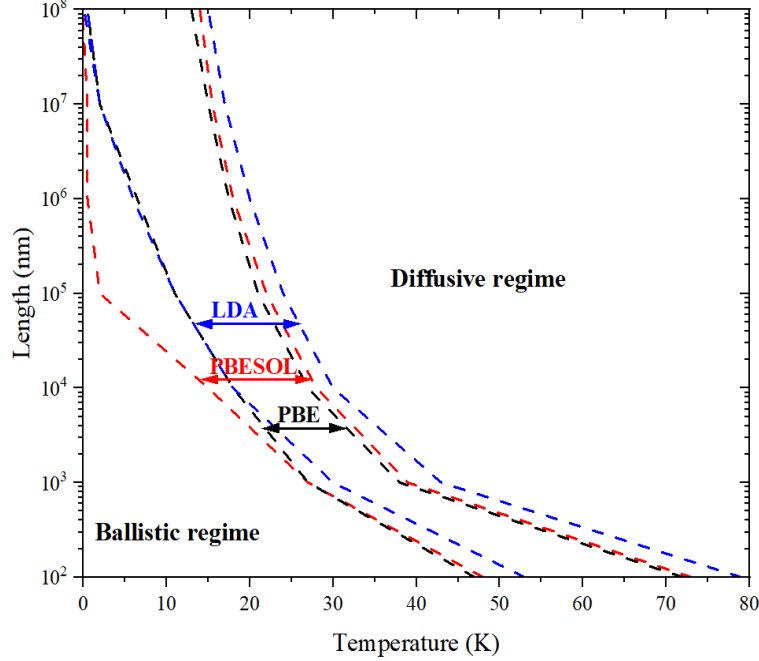


FIG. 4. Thermal transport regimes for NaF: phonon hydrodynamics regime, ballistic regime, and diffusive regime. Double arrow lines show the window of phonon hydrodynamics for each functional. PBE (black dashed lines), PBESOL (red dashed lines), and LDA (blue dashed lines).

B. Properties of LiF

Following the same procedure that was used for NaF, in order to obtain the ground state energy for PBE, PBESOL, and LDA, the lattice constant (a) was adjusted by relaxing the LiF structure. The calculated lattice constant for PBE ($a_{\text{PBE}} = 4.07 \text{ \AA}$) is greater than the experimental value ($a_{\text{exp}} = 4.02 \text{ \AA}$) that was found from the typical incident angular scan in the $\{100\}$ direction [51], while the calculated lattice constants for PBESOL ($a_{\text{PBESOL}} = 4.01 \text{ \AA}$) and LDA ($a_{\text{LDA}} = 3.91 \text{ \AA}$) are smaller compared to the experimental value. As in the case of NaF, the LO-TO splitting value is determined based on the Born effective charge (Z^*) calculation. The calculated Z^* for PBE and PBESOL was computed to be identically 1.05 and -1.05 for Li and F elements, respectively, and using LDA was found to be 1.04 and -1.04 for Li and F elements, respectively. From Table IV, the frequencies for the LO-TO splitting ($\omega_{\text{LO}} - \omega_{\text{TO}}$) at the gamma point are 10.53, 10.12, and 9.81 THz for PBE, PBESOL, and LDA, respectively, which are in good agreement with the experimental value ($\omega_{\text{exp}} = 10.55 \text{ THz}$) [52]. The greatest band gap value of LiF was obtained using the LDA functional ($E_g = 9.64 \text{ eV}$), yet it is less than the experimental values with an error of $\sim 41\%$ [53,54]. However, the calculated value for the valence bandwidth using LDA is 3.5 eV, which is identical to the measured bandwidth of 3.5 eV in Ref. [55].

Table IV. Lattice constant a (Å), dielectric constant ϵ , Born effective charge Z^* , phonon frequencies at gamma ω (THz), and band gap E_g (eV) of calculated, other theoretical data, and experimental data for LiF.

	PBE	PBESOL	LDA	Other theoretical data	Experiments
a	4.07	4.01	3.91	3.886 ^{a1} , 4.005 ^{a2} , 4.002 ^{b1} , 4.103 ^{b2} , 4.02 ^c , 4.07 ^d	4.02 ^e , 3.99 ^f
ϵ	2.04	2.08	2.11	2.04 ^b , 2.19 ^g	1.93 ^h
Z^*	1.05	1.05	1.04	1.03 ^b , 1.06 ^d , 0.998 ⁱ	-
ω_{LO}	18.63	19.18	20.09	19.89 ^b , 19.92 ^d ,	19.70 ^j
ω_{TO}	8.09	9.06	10.28	10.61 ^b , 10.29 ^d ,	9.15 ^j
E_g	8.82	9.04	9.64	8.727 ^d , 7.64 ^{k1} , 9.15 ^{k2} , 8.7 ^l	13.6 ^m , 14.2 ⁿ

^{a1}Ref. [56], calculated using LDA. ^{a2}Ref. [56], calculated using GGA. ^bRef. [24]. ^{b1}Ref. [24], calculated using LDA. ^{b2}Ref. [24], calculated using GGA. ^cRef. [31]. ^dRef. [57]. ^eRef. [51]. ^fRef. [58]. ^gRef. [59]. ^hRef. [34]. ⁱRef. [35]. ^jRef. [52]. ^{k1}Ref. [60], calculated using LDA. ^{k2}Ref. [60], calculated using PBE. ^lRef. [61], calculated using LDA. ^mRef. [53]. ⁿRef. [54].

As LiF shares the same crystal symmetry as NaF, the presented phonon dispersion relations of LiF, Fig. 5 (a), follow the same symmetrical directions in the Brillouin zone as NaF. The calculated longitudinal optical mode (LO) values using LDA functional are consistent with Ref. [52], while the calculated transverse optical modes (TO) values using the PBESOL functional are in good agreement with the measured value of the same reference. From the dispersion relations of LiF, the transverse optical modes (TO₁, TO₂) are doubly degenerate at the gamma point. From the LDA functional dispersion curves, the longitudinal optical mode (LO) of LiF reaches a frequency of ~ 20 THz at the Gamma point, a greater value than the LO mode's frequency of NaF (~ 11.7 THz) using the PBE functional.

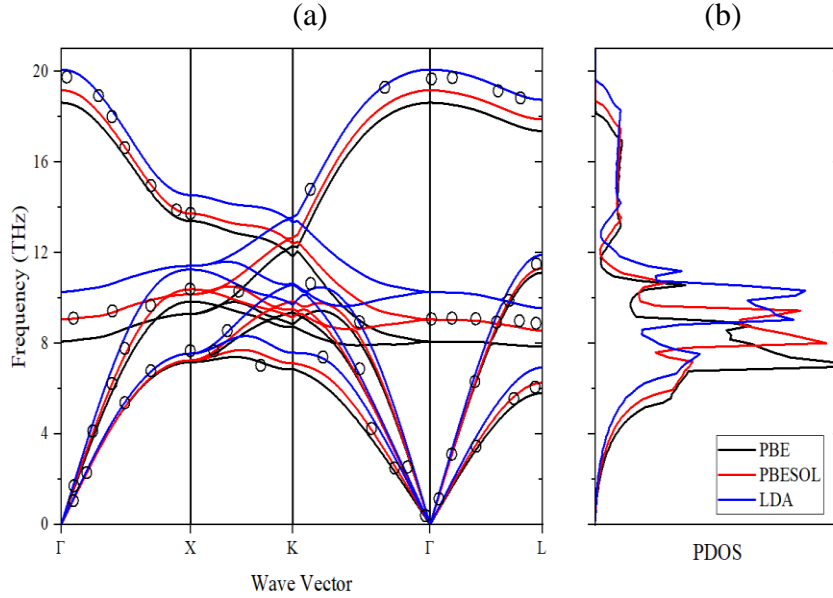


FIG. 5. (a) Calculated phonon dispersion and (b) phonon density of states for LiF. Calculations were done with PBE (black solid lines), PBESOL (red solid lines), and LDA (blue solid lines). Black circles are the measured data from Ref. [52].

The calculated bulk modulus and elastic constants of LiF are shown in Table V. There are four conditions for the mechanical stability of the elastic constants in cubic crystals, which are: $C_{11} > 0$, $C_{44} > 0$, $C_{11} - C_{12} > 0$, and $C_{11} + 2C_{12} > 0$ [57]. The values of the elastic constants for fluoride materials (NaF and LiF) satisfy all these conditions. Comparing theoretical elastic constants with experiments is challenging because of the uncertainties in experimentally determining C_{12} , which is a linear combination of the elastic constants in the $\{110\}$ direction, whereas C_{11} and C_{44} values can be measured directly by ultrasonic techniques [62]. Nevertheless, our C_{12} value ($C_{12} = 50.61$ GPa) with LDA agrees with the experimental value of 47.4 GPa [40], with an error of 6.75 %.

Table V. Bulk modulus B (GPa) and elastic constants C_{ij} (GPa) of calculated, other theoretical data, and experimental data for LiF.

	PBE	PBESOL	LDA	Other theoretical data	Experiments
B	67.17	72.55	86.78	67.71 ^{a1} , 73.59 ^{a2} , 72.99 ^{b1} , 70.53 ^{b2} , 87.1125 ^c , 76.1 ^d	76.9 ^e
C_{11}	109.45	126.71	143.12	153.15 ^b , 129.1 ^d	135.8 ^e
C_{12}	46.03	45.48	50.61	45.62 ^b , 49.5 ^d	47.4 ^e

C_{44}	60.32	61.91	68.07	55.08 ^b , 49.5 ^d	68.7 ^e
----------	-------	-------	-------	--	-------------------

^{a1}Ref. [24], calculated using GGA, ^{a2}Ref. [24], calculated using LDA. ^bRef. [57]. ^{b1}Ref. [57], calculated using Birch-Murnaghan EOS. ^{b2}Ref. [57], calculated using Vinet EOS. ^cRef. [42]. ^dRef. [62]. ^eRef. [40].

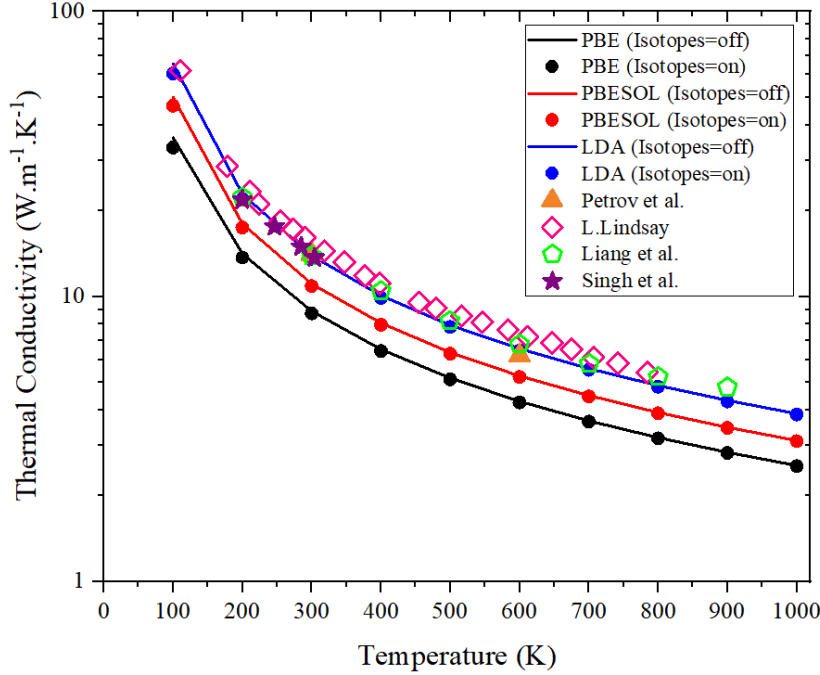


FIG. 6. Calculated lattice thermal conductivity for LiF. Calculations were done with PBE (black solid line), PBESOL (red solid line), and LDA (blue solid line). Calculations show the effect of the isotopes on the thermal conductivity: PBE (black circles), PBESOL (red circles), and LDA (blue circles). Experimental data: Ref. [63] (orange triangles). Theoretical data: Ref. [56] (pink diamonds), Ref. [24] (green pentagons), Ref. [64] (purple stars).

The effect of isotopes on the thermal conductivity calculations for LiF is shown in Fig. 6. The isotopic composition of the lithium in LiF reflects the natural abundance of Li-6 and Li-7 which corresponds to 7.42% and 92.58% respectively. The difference between the thermal conductivity values of pure LiF and impure LiF (with isotopes) is small ($< 3\%$). The calculated thermal conductivity for pure LiF using LDA ($k = 13.91 \text{ W.m}^{-1}.\text{K}^{-1}$) at room temperature is close to the measured value ($k_{\text{exp}} = 14.09 \text{ W.m}^{-1}.\text{K}^{-1}$) by Petrov *et al.* [63] with an error of 1.28 %, whereas the calculated thermal conductivity, including the isotopes, is $13.56 \text{ W.m}^{-1}.\text{K}^{-1}$ with an error of 3.76 %. Furthermore, the percentage errors of calculated specific heat ($c_p = 1.55 \text{ kJ.kg}^{-1}.\text{K}^{-1}$), average Grüneisen parameter ($\bar{\gamma} = 1.54$), and density ($\rho = 2.88 \text{ g.cm}^{-3}$) at room temperature

using LDA for pure LiF are 0.65, 3.14, and 10.77 %, respectively, compared to experimental results [49,65,66].

Table VI. Thermal conductivity k ($\text{W}\cdot\text{m}^{-1}\cdot\text{K}^{-1}$), specific heat c_p ($\text{kJ}\cdot\text{kg}^{-1}\cdot\text{K}^{-1}$), average Grüneisen parameter $\bar{\gamma}$, and density ρ ($\text{g}\cdot\text{cm}^{-3}$) of calculated, other theoretical data, and experimental data for LiF at room temperature.

	PBE	PBESOL	LDA	Other theoretical data	Experiments
k	8.88	11.07	13.91	14.59 ^{a1} , 22.42 ^{a2} 13.89 ^{b1} , 13.48 ^{b2} , 14.80 ^c , 13.60 ^d	14.09 ^e
c_p	1.62	1.59	1.55	1.62 ^f	1.54 ^f
$\bar{\gamma}$	2.08	1.88	1.54	1.24 ^{b1} , 1.36 ^{b2}	1.59 ^g
ρ	2.56	2.67	2.88	-	2.60 ^h

^{a1}Ref. [56], calculated using $a_0 = 3.894 \text{ \AA}$. ^{a2}Ref. [56], calculated using $a(300 \text{ K}) = 4.004 \text{ \AA}$.
^{b1}Ref. [24], calculated using $a_0 = 4.002 \text{ \AA}$. ^{b2}Ref. [24], calculated using $a(300 \text{ K}) = 4.03 \text{ \AA}$.
^cRef. [67]. ^dRef. [64]. ^eRef. [63]. ^fRef. [49]. ^gRef. [65], given at $T = 323.15 \text{ K}$. ^hRef. [66].

In the context of phonon hydrodynamics, our findings reveal that LiF exhibits a significantly wider temperature-length window for phonon hydrodynamics than NaF, and the variation between functionals is greater, as demonstrated in Fig. 7.

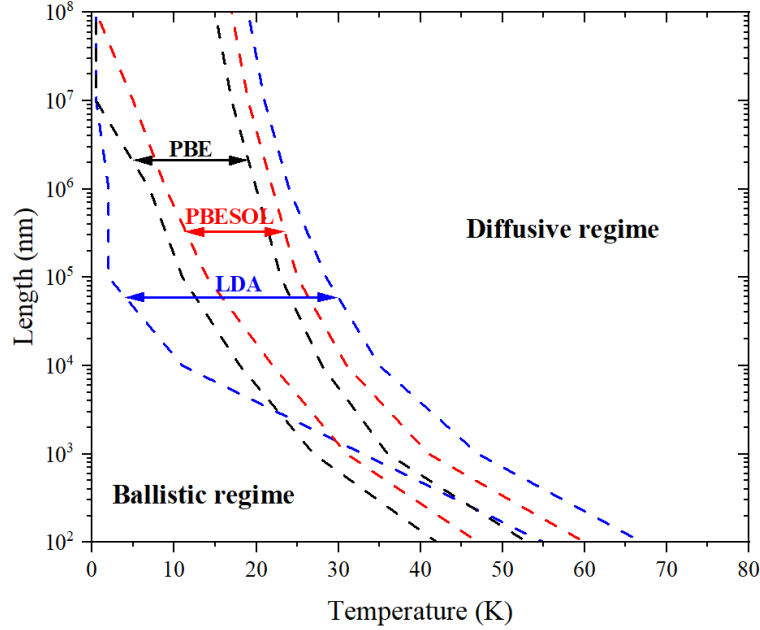


FIG. 7. Thermal transport regimes for LiF: phonon hydrodynamics regime, ballistic regime, and diffusive regime. Double arrow lines show the window of phonon hydrodynamics for each functional. PBE (black dashed lines), PBESOL (red dashed lines), and LDA (blue dashed lines).

C. Properties of LiH

For LiH, the calculated lattice constants using PBE, PBESOL, and LDA functionals ($a_{\text{PBE}} = 4.01 \text{ \AA}$, $a_{\text{PBESOL}} = 3.98 \text{ \AA}$, and $a_{\text{LDA}} = 3.91 \text{ \AA}$) are all in close agreement with the experimental values ($a_{\text{exp1}} = 4.069 \text{ \AA}$ [68] and $a_{\text{exp2}} = 4.083 \text{ \AA}$ [69]) with an error of less than 5 %. The experimental born effective charge of LiH ($Z_{\text{exp1}}^* = 0.991$) was computed by Shukla [35] using experimental values of the Szigeti charge ‘ Z_s ’ and the high-frequency dielectric constant ‘ ϵ_∞ ’ from Ref. [70] and applying the relation of $Z^* = [(\epsilon_\infty + 2)/3]Z_s$, which is described in Ref. [71]. This computed value and the experimental value ($Z_{\text{exp2}}^* = 1.11$ [72]) agree with our results. From Table VII, the frequency of LO is much higher than TO due to the strong depolarization field in LiH. The LO frequency at the gamma point can also be obtained from the Lyddane-Sachs-Teller (LST) relation ($\omega_{\text{LO}}^2 / \omega_{\text{TO}}^2 = \epsilon_0 / \epsilon_\infty$) [73], which gives a value of 32.40 THz. ϵ_0 refers to the static dielectric constant. Both values from first-principles calculations and the LST relation agree the experimental values [68,70,72,74].

Table VII. Lattice constant a (Å), dielectric constant ϵ , Born effective charge Z^* , phonon frequencies at gamma ω (THz), and band gap E_g (eV) of calculated, other theoretical data, and experimental data for LiH.

	PBE	PBESOL	LDA	Other theoretical data	Experiments
a	4.01	3.98	3.91	3.947 ^{a1} , 3.894 ^{a2} , 4.02 ^b , 3.997 ^c	4.069 ^d , 4.083 ^e , 4.083 ^f , 4.083 ^g
ϵ	4.39	4.70	4.99	4.34 ^b , 4.81 ^h	3.61 ^e
Z^*	1.02	1.02	1.03	1.020 ^c , 1.03 ^h , 1.046 ⁱ	0.991 ^j , 1.11 ^h
ω_{LO}	32.43	32.37	32.96	28.3 ^h	32.21 ^d , 33.50 ^h , 33.60 ^j , 33.15 ^k
ω_{TO}	17.56	18.52	19.41	18.1 ^h , 17.86 ^l	18.14 ^d , 18.40 ^h , 17.76 ^j , 17.70 ^k
E_g	2.98	2.73	2.54	3.00 ^{b1} , 2.61 ^{b2} , 4.75 ^{b3} , 2.53 ^l	5.00 ^m , 4.92 ⁿ

^{a1}Ref. [56], calculated using GGA. ^{a2}Ref. [56], calculated using LDA. ^bRef. [75]. ^{b1}Ref. [75], calculated using GGA. ^{b2}Ref. [75], calculated using LDA. ^{b3}Ref. [75], calculated using GW. ^cRef. [76]. ^dRef. [68]. ^eRef. [69]. ^fRef. [77]. ^gRef. [78]. ^hRef. [72]. ⁱRef. [35]. ^jRef. [70]. ^kRef. [74]. ^lRef. [79]. ^mRef. [80]. ⁿRef. [81].

The calculated phonon dispersion of LiH along the high-symmetry directions is plotted in Fig. 8 (a). The phonon dispersion curves of alkali hydrides (LiH, NaH) are characterized by a gap existing between the acoustic and optical modes. The acoustic – optical ($a-o$) gap can be attributed to the mass variation between the constituent elements [56,82]. The acoustic-optical gap influences three-phonon scattering by determining the energy range over which transitions between the acoustic and optical phonon modes can occur. For instance, the three optical phonon scattering processes (ooo) in LiH are forbidden due to energy conservation [83]. The bunching of the acoustic branches can be calculated at the X point through $(\omega_{LA} - \omega_{TA}) / \omega_{LA}$. This relation gives values of 0.24, 0.25, and 0.26 for PBE, PBESOL, and LDA, respectively, which is in good accordance with the calculated value of 0.23 [56]. Also, this results in values of 0.26 and 0.24 for LiF, and NaH, respectively, but NaF has a greater value of 0.43, indicating an effect of (aaa) scattering. For LiH, the phonon dispersion obtained using the PBE functional is consistent with Ref. [68]. It is noted that TO_2 breaks up from TO_1 and degenerates with LO at the K wave vector.

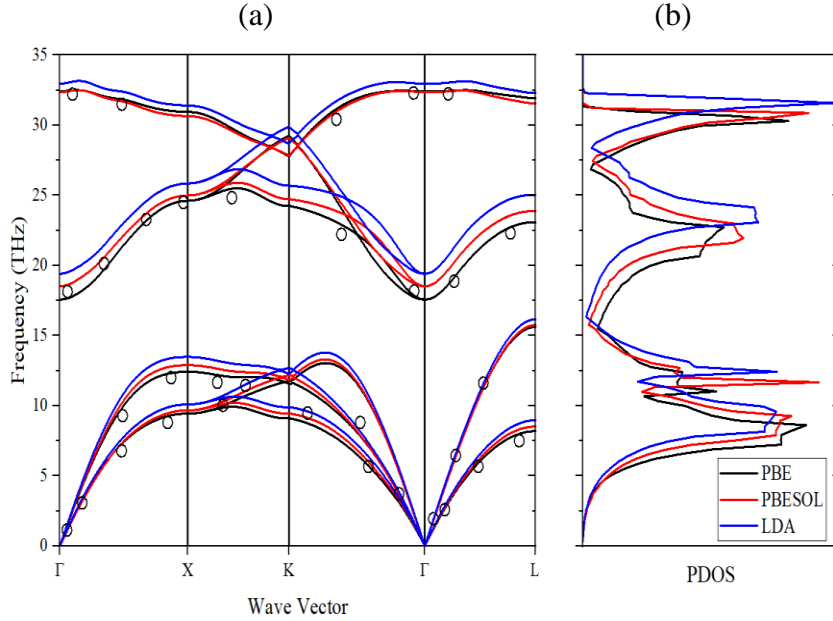


FIG. 8. (a) Calculated phonon dispersion and (b) phonon density of states for LiH. Calculations were done with PBE (black solid lines), PBESOL (red solid lines), and LDA (blue solid lines). Black circles are the measured data from Ref. [68].

The experimental and first-principles data for the elastic constants of LiH is shown in Table VIII. A mechanical parameter of interest for alkali hydrides (LiH, NaH) is the elastic anisotropy factor ‘AF’. The degree of anisotropy is based on the magnitude of the directional dependence of the properties [84]. $AF = 2C_{44}/(C_{11}-C_{12})$, where $AF = 1$ for an elastic isotropic medium [85]. AF values of LiH with PBE, PBESOL, and LDA are 1.65, 1.29, and 1.21, respectively. Like LiH, LiF also has a large AF value ($AF = 1.90$ using PBE). These values indicate a strong elastic anisotropy in these materials. One interesting consequence of elastic anisotropy is the phenomenon of long-wavelength phonon focusing [86]. At high AF, it is expected a strong phonon focusing effect will occur even at the long-wavelength elastic limit. It has further been suggested that phonon focusing may be connected to phonon hydrodynamics in fluorides and alkali hydrides because phonon focusing occurs at the same low temperatures where phonon hydrodynamics has been observed [87].

Table VIII. Bulk modulus B (GPa) and elastic constants C_{ij} (GPa) of calculated, other theoretical data, and experimental data for LiH.

	PBE	PBESOL	LDA	Other theoretical data	Experiments
B	34.24	37.06	40.60	34.03 ^{a1} , 41.33 ^{a2} , 36.6 ^b , 36.07 ^c	34.24 ^b , 31.7 ^d
C_{11}	73.06	85.34	95.36	78.9 ^e , 79.8 ^f , 65.82 ^g	74.10 ^f , 67.20 ^h
C_{12}	14.03	10.42	10.22	44.3 ^e , 45.9 ^f , 15.44 ^g	14.20 ^f , 14.93 ^h
C_{44}	48.62	48.31	51.48	44.1 ^e , 45.7 ^f , 42.91 ^g	48.40 ^f , 46.37 ^h

^{a1}Ref. [88], calculated using PBE. ^{a2}Ref. [88], calculated using LDA. ^bRef. [89]. ^cRef. [90]. ^dRef. [91]. ^eRef. [92]. ^fRef. [93]. ^gRef. [94]. ^hRef. [95]

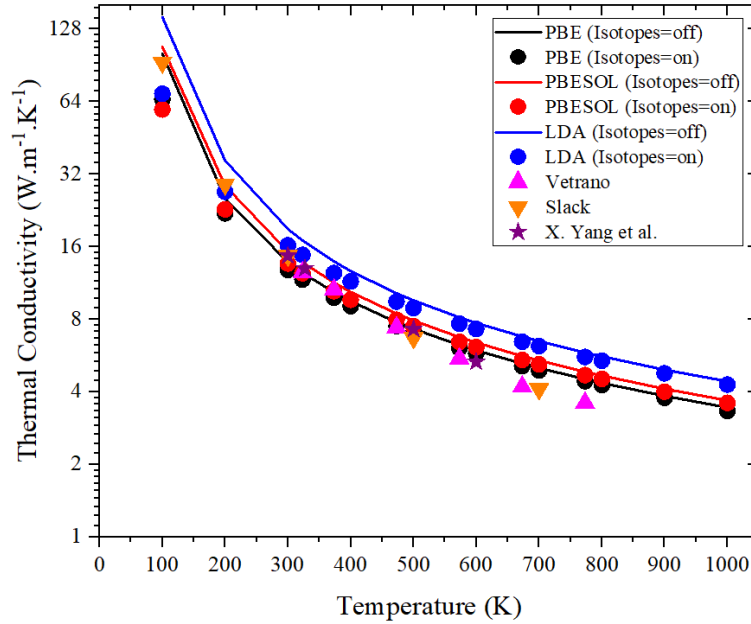


FIG. 9. Calculated lattice thermal conductivity for LiH. Calculations were done with PBE (black solid line), PBESOL (red solid line), and LDA (blue solid line). Calculations show the effect of the isotopes on the thermal conductivity: PBE (black circles), PBESOL (red circles), and LDA (blue circles). Experimental data: Ref. [96] (pink up triangles), Ref. [97] (orange down triangles). Theoretical data: Ref. [76] (purple stars).

Several experiments and theoretical calculations have been performed to determine the thermal conductivity of LiH [56,76,96,97], as shown in Fig. 9. Vetrano [96] measured the thermal conductivity of LiH at $T = 327$ K ($k_{\text{exp}} = 12.47$ W.m⁻¹.K⁻¹). Referring to Table IX, previous theoretical studies yielded higher thermal conductivity values at the same temperature [56,76].

Our calculations using PBE are in good agreement with Vatrano's value if the effect of isotopes is excluded. Including isotopes in our calculations leads to an increase in the error percentage to 6 %. Specific heat value ($c_p = 3.69 \text{ kJ.kg}^{-1}.\text{K}^{-1}$) with PBE is also in good agreement with the experiment value ($c_p = 3.64 \text{ kJ.kg}^{-1}.\text{K}^{-1}$) [98]. LiH has a relatively low density ($\rho \approx 0.775 \text{ g.cm}^{-3}$ by experiments [69,70,77]) and, again, our calculated density values using PBE agree with these experiments. Phonon hydrodynamic windows for LiH can be shown in Fig. 10. As was found in the case NaF and LiF, LDA yields the widest phonon hydrodynamic window in LiH.

Table IX. Thermal conductivity k ($\text{W.m}^{-1}.\text{K}^{-1}$), specific heat c_p ($\text{kJ.kg}^{-1}.\text{K}^{-1}$), average Grüneisen parameter $\bar{\gamma}$, and density ρ (g.cm^{-3}) of calculated, other theoretical data, and experimental data for LiH at room temperature.

	PBE	PBESOL	LDA	Other theoretical data	Experiments
k^*	12.47	13.76	16.98	25.51 ^{a1} , 23.00 ^{a2} , 12.98 ^b	12.47 ^c
c_p	3.69	3.57	3.45	-	3.64 ^d
$\bar{\gamma}$	1.64	1.57	1.42	1.64 ^e	1.28 ^f
ρ	0.81	0.84	0.88	-	0.775 ^g , 0.775 ^h , 0.7754 ⁱ

*Thermal conductivity values were obtained at $T = 327 \text{ K}$, except ^{a1}Ref. [56] calculated using $a_0 = 3.894 \text{ \AA}$, and ^{a2}Ref. [56] calculated using $a(300 \text{ K}) = 4.004 \text{ \AA}$. ^bRef. [76]. ^cRef. [96]. ^dRef. [98]. ^eRef. [99]. ^fRef. [95]. ^gRef. [69]. ^hRef. [77]. ⁱRef. [70].

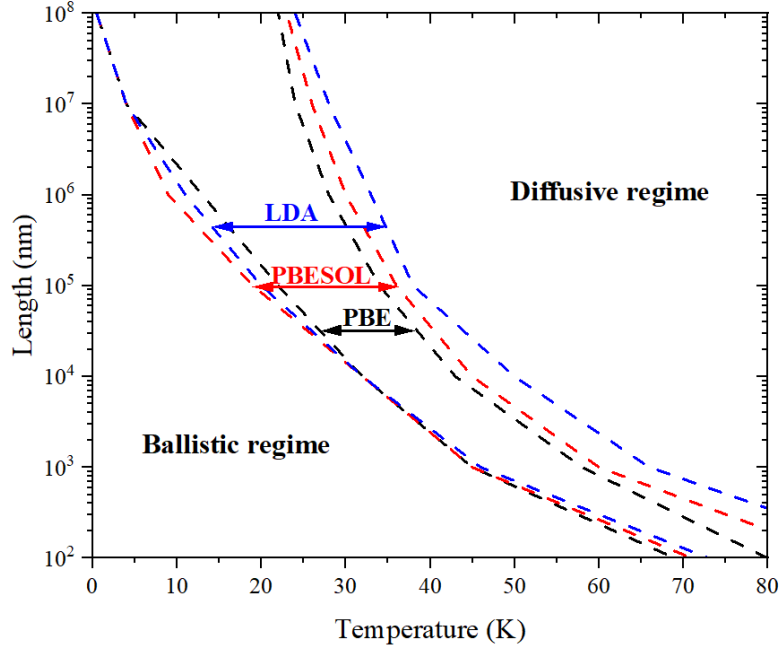


FIG. 10. Thermal transport regimes for LiH: phonon hydrodynamics regime, ballistic regime, and diffusive regime. Double arrow lines show the window of phonon hydrodynamics for each functional. PBE (black dashed lines), PBESOL (red dashed lines), and LDA (blue dashed lines).

D. Properties of NaH

The calculated lattice constant with PBE ($a_{\text{PBE}} = 4.84 \text{ \AA}$), from Table X, is the closest to the experimental value ($a_{\text{exp}} = 4.88 \text{ \AA}$) [100], where the error is less than 1 %. From Sec.III in the Supplemental Material, the bandwidths in LiH are larger than those in NaH due to the near distance of the hydrogen atoms [75]. Moreover, the two materials have different types of electronic band gaps. For LiH, as shown in Fig. 11 (a), the minimum energy gap between the conduction and valence bands are at the X point (circled in red). Unlike LiH, the band gap in NaH is indirect. For NaH, as seen in Fig. 11 (b), the minimum energy gap occurs between the conduction band at L point and the valence band at X point (red double arrow). It is noted that the LO-TO splitting frequencies value of NaH ($\omega_{\text{LO-TO}} = 11.78 \text{ THz}$ using PBE) and LiH ($\omega_{\text{LO-TO}} = 14.87 \text{ THz}$ using PBE) are greater than the LO-TO splitting frequencies value of NaF ($\omega_{\text{LO-TO}} = 4.89 \text{ THz}$ using PBE) and LiF ($\omega_{\text{LO-TO}} = 9.81 \text{ THz}$ using LDA) at the gamma point. The large LO-TO splitting frequency values are due to strong polar phonon (creation of an oscillating electric field inside a crystal caused by phonons due to local charge polarization [101]) frequencies of hydride materials (LiH, NaH) compared to fluoride materials (NaF, LiF).

Table X. Lattice constant a (Å), dielectric constant ϵ , Born effective charge Z^* , phonon frequencies at gamma ω (THz), and band gap E_g (eV) of calculated, other theoretical data, and experimental data for NaH.

	PBE	PBESOL	LDA	Other theoretical data	Experiments
a	4.84	4.79	4.69	4.82 ^a , 4.83 ^b , 4.83 ^c , 4.862 ^d	4.88 ^e
ϵ	3.13	3.26	3.36	3.09 ^a , 3.06 ^c	-
Z^*	0.97	0.96	0.95	0.96 ^a , 0.97 ^b	-
ω_{LO}	26.75	26.65	27.52	$\sim 27.06^b$	-
ω_{TO}	14.97	15.44	16.83	16.6 ^{f1} , 13.9 ^{f2}	-
E_g	3.76	3.61	3.55	4.90 ^a , 3.79 ^{c1} , 3.42 ^{c2} , 5.87 ^{c3} , 5.68 ^{g1} , 3.39 ^{g2}	-

^aRef. [102]. ^bRef. [103]. ^cRef. [75]. ^{c1}Ref. [75], calculated using GGA. ^{c2}Ref. [75], calculated using LDA. ^{c3}Ref. [75], calculated using GW. ^dRef. [104]. ^eRef. [100]. ^{f1}Ref. [105], calculated using clamped-nucleus (CN) approximation. ^{f2}Ref. [105], calculated using quasiharmonic (QH) approximation. ^{g1}Ref. [106], calculated using GW. ^{g2}Ref. [106], calculated using LDA.

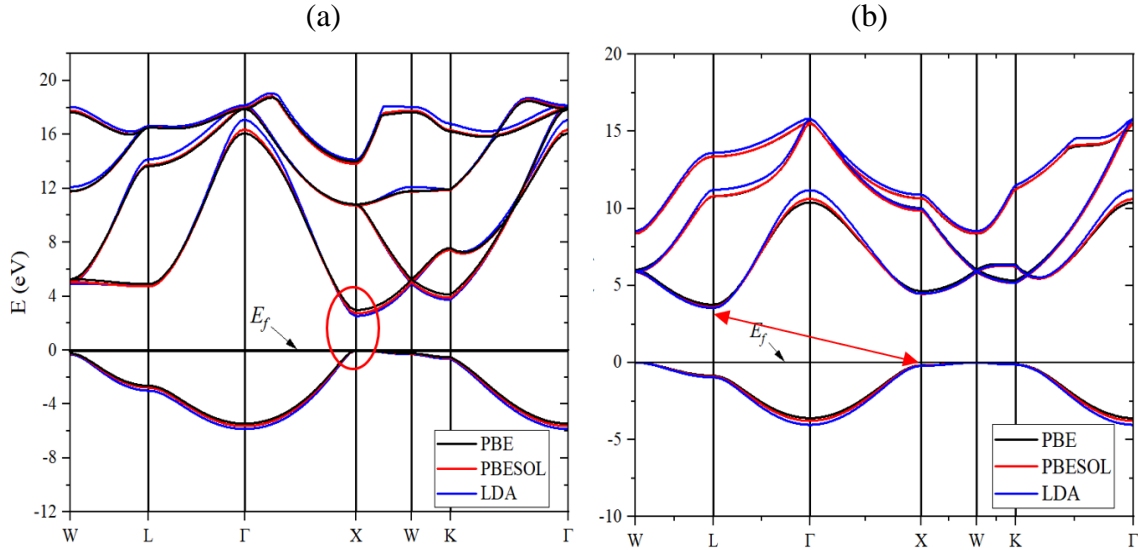


FIG. 11. Electronic band structures of: (a) LiH. (b) NaH. Fermi energy (E_f) is set at 0 eV.

As shown in Fig. 12 (a), the (*a-o*) gap in NaH is greater than the (*a-o*) gap in LiH because of the large mass difference between ‘Na’ and ‘H’ atoms in contrast to ‘Li’ and ‘H’ atoms. This gap is clearly visible in the PDOS, as shown in Fig. 12 (b). The calculated (*a-o*) gap is about 7.83, 8.27, and 9.43 THz using PBE, PBESOL, and LDA, respectively. Zhao *et al.* [103] calculated the gap value for NaH, (*a-o*) gap = 49.3 rad/ps \approx 7.85 THz, close to the PBE value. The PDOS reveals that the sodium atoms provide practically all of the acoustic vibrations, whilst the hydrogen atoms are the source of the majority of the optical modes [103]. According to the PDOS diagram (Fig. 12 (b)), the highest frequency for hydrogen atom vibrations is about 26.7 THz using PBE, consistent with what was found in Ref. [102].

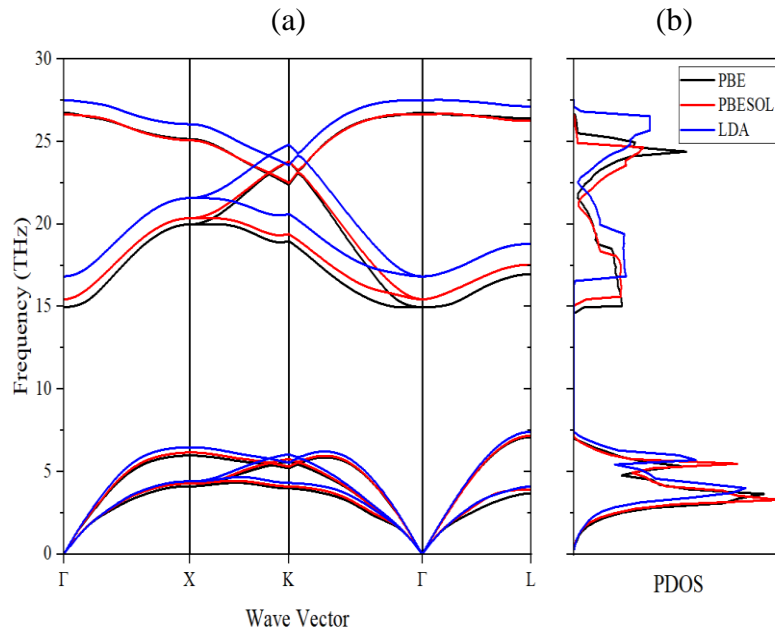


FIG. 12. (a) Calculated phonon dispersion and (b) phonon density of states for NaH. Calculations were done with PBE (black solid lines), PBESOL (red solid lines), and LDA (blue solid lines).

Table XI presents the elastic constants of NaH. One can inspect the elastic constants data to see whether the material is brittle or ductile. According to Cauchy pressure ($C_{12} - C_{44}$), if the difference is positive, the material is ductile; otherwise, it is brittle [107]. All materials (NaF, LiF, and LiH) were discussed so far are brittle (negative difference). Another criterion for checking the ductility/brittleness of materials is Pugh's modulus ratio (B/G), where G is the shear modulus [108]. The critical value of Pugh's modulus ratio is 1.75. If the ratio > 1.75 , the material is ductile; otherwise, it is brittle [109]. This ratio gives 1.18, 1.17, and 1.20 for PBE, PBESOL, and LDA, respectively, indicating that NaH is brittle. Other materials, such as silicon and germanium, are brittle as well [110].

Table XI. Bulk modulus B (GPa) and elastic constants C_{ij} (GPa) of calculated, other theoretical data, and experimental data for NaH.

	PBE	PBESOL	LDA	Other theoretical data	Experiments
B	22.16	23.92	27.43	22.90 ^a , 22.93 ^b , 23.7 ^c , 27 ^{d1} , 20 ^{d2}	19.40 ^e 14.30 ^f
C_{11}	43.69	47.19	55.25	42.12 ^b , 47.3 ^g	-
C_{12}	12.89	12.29	13.52	13.06 ^b , 22.5 ^g	-
C_{44}	22.35	22.31	24.19	22.02 ^b , 22.5 ^g	-

^aRef. [111]. ^bRef. [104]. ^cRef. [112]. ^{d1}Ref. [105], calculated using clamped-nucleus (CN) approximation. ^{d2}Ref. [105], calculated using quasiharmonic (QH) approximation. ^eRef. [113]. ^fRef. [114]. ^gRef. [92].

In Table XII, the calculated thermal conductivity and experimental values of NaH at room temperature are reported [115]. LDA yields a less accurate prediction when compared with the predictions from the PBE and PBESOL functionals. The calculated thermal conductivity values of NaH, shown in Fig. 13, are less than LiH, NaF, and LiF, with values between 1 and 40 $\text{W}\cdot\text{m}^{-1}\cdot\text{K}^{-1}$ for temperature ranges between 100 and 1000 K. The difference between the thermal conductivity values using the PBE and PBESOL functionals is almost negligible.

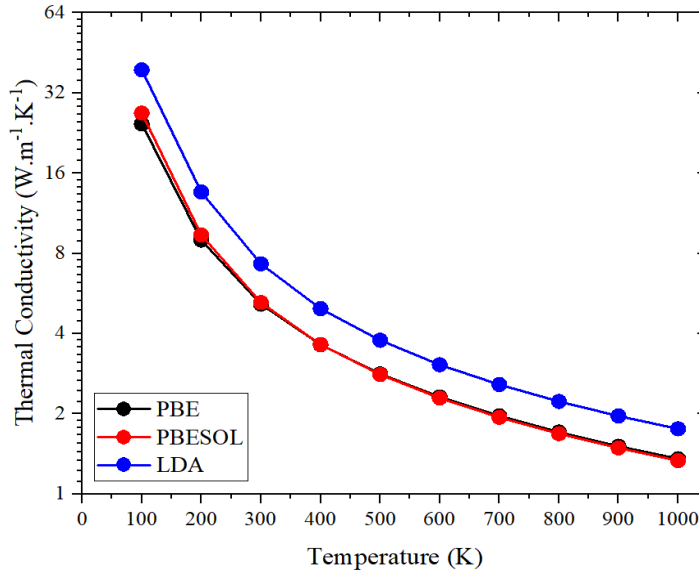


FIG. 13. Calculated lattice thermal conductivity for NaH. Calculations were done with PBE (black circles), PBESOL (red circles), and LDA (blue circles).

Table XII. Thermal conductivity k ($\text{W}\cdot\text{m}^{-1}\cdot\text{K}^{-1}$), specific heat c_p ($\text{kJ}\cdot\text{kg}^{-1}\cdot\text{K}^{-1}$), average Grüneisen parameter $\bar{\gamma}$, and density ρ ($\text{g}\cdot\text{cm}^{-3}$) of calculated, other theoretical data, and experimental data for NaH at room temperature.

	PBE	PBESOL	LDA	Other theoretical data	Experiments
k	5.16	5.23	7.30	15.41 ^a	5.00 ^b
c_p	1.51	1.52	1.46	-	1.52 ^c
$\bar{\gamma}$	1.68	1.77	1.65	1.8 ^{d1} , 2.2 ^{d2} , 1.76 ^e	-
ρ	1.41	1.44	1.54	-	1.39 ^f , 1.37 ^g

^aRef. [103]. ^bRef. [115]. ^cRef. [116]. ^{d1}Ref. [105], calculated using clamped-nucleus (CN) approximation. ^{d2}Ref. [105], calculated using quasiharmonic (QH) approximation. ^eRef. [99]. ^fRef. [117]. ^gRef. [118].

Based on our calculations, the difference in magnitude between N-scattering and U-scattering rates in NaH is not as significant as compared to NaF, LiF, and LiH (see Sec.IV of the Supplemental Material) and the resulting phonon hydrodynamics window for different characteristic lengths exhibit is narrow, as shown in Fig. 14.

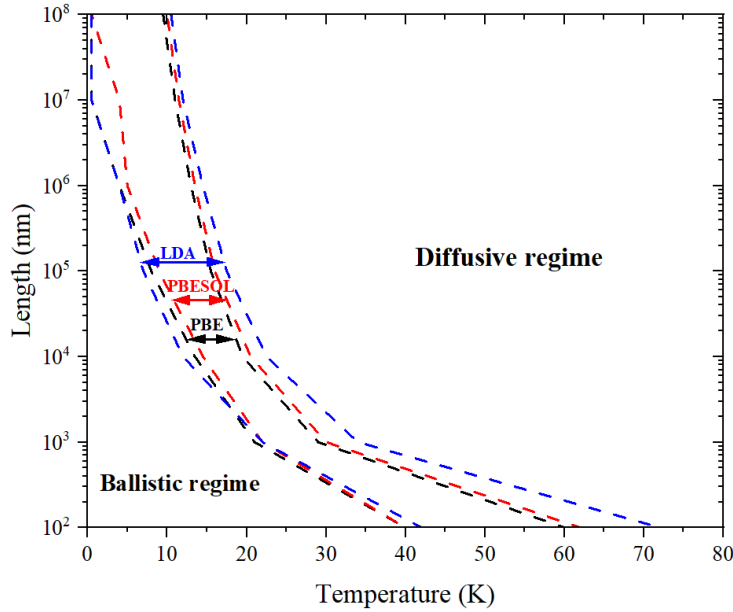


FIG. 14. Thermal transport regimes for NaH: phonon hydrodynamics regime, ballistic regime, and diffusive regime. Double arrow lines show the phonon hydrodynamics range for each functional. PBE (black dashed lines), PBESOL (red dashed lines), and LDA (blue dashed lines).

Finally, we briefly comment on the impact of isotopes on the phonon hydrodynamics windows. For LiF (Fig. 15 (b) in the Supplemental Material), the resistive scattering rate (R-scattering) can be used instead of U-scattering to predict phonon hydrodynamics (applying Eq. 2.). Using R-scattering, the hydrodynamics window range of LiF narrows to 9 K (shaded red region), compared with U-scattering, which extends up to 24.5 K (shaded transparent red region). On the other hand, for NaF and NaH (Fig. 15 (a) and (d) in the Supplemental Material), the curves of U-scattering and R-scattering remain close to each other, and consequently, the hydrodynamics windows are nearly the same. Importantly, the hydrodynamic windows disappear for LiH, Si, and Ge if isotope scattering is included, as illustrated in Fig. 15 (c), (e), and (f). Fig. 16 (Supplemental Material) shows the phonon thermal transport regimes for NaF, LiF, and NaH including isotope scattering. While the phonon thermal transport regimes in NaF and NaH remain unaffected by isotopes, the influence of isotopes on LiF is clear, particularly when using LDA, as shown in Fig. 16 (b) - Supplemental Material.

IV. DISCUSSION

To reconcile the observation that the calculations of electronic band gap deviate significantly from experimental values while better agreement is obtained for phonon properties, several paths forward exist. For instance, Becke and Johnson (BJ) exchange potential was proposed to precisely regenerate the exact atomic exchange optimized effective potential (OEP) potential in terms of shape, resulting in accurate calculated electronic band gaps [119]. The HSE (Heyd-Scuseria-Ernzerhof) hybrid functional [120] is another functional that has been shown to improve electronic properties such as band gaps. It combines the traditional DFT exchange-correlation functional with a fraction of Hartree-Fock (HF) exchange [120] via a mixing parameter that determines the contribution of HF exchange to the total exchange-correlation energy. However, this functional requires greater computational resources than the simple PBE functional. We tested PBE with HSE in LiF and found that the band gap increased to 11.17 eV with an error of $\sim 18\%$. Since HSE functional is not presently implemented within the `ph.x` package of Quantum ESPRESSO, Phonopy [121,122] and Phono3py [121,122] are employed to calculate the second and third interatomic force constants, respectively. Fig. 15 displays the phonon dispersion and phonon DOS for LiF using simple PBE and PBE with HSE. While PBE+HSE improves the band gap prediction, it does not significantly change the phonon dispersion.

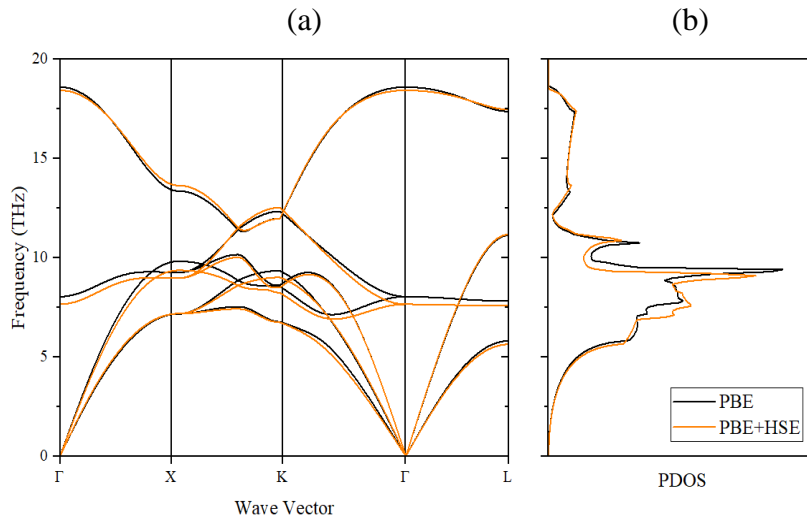


FIG. 15. (a) Calculated phonon dispersion and (b) phonon density of states for LiF. Calculations were done with PBE (black solid lines) and PBE with HSE (orange solid lines).

To ensure a fair comparison regarding thermal conductivity and phonon hydrodynamics windows between PBE and PBE+HSE, as shown in Fig. 16 and 17 while remaining within reasonable computational costs, we consistently applied a $2 \times 2 \times 2$ supercell for calculating both the second and third interatomic force constants in each case. In our analysis of LiF's thermal transport regimes using both PBE and PBE-HSE functionals, we found similar results under the same conditions, with larger differences emerging at higher temperatures. However, when we compared predictions from PBE calculations using a supercell that ensures converged phonon properties, clear differences can be seen.

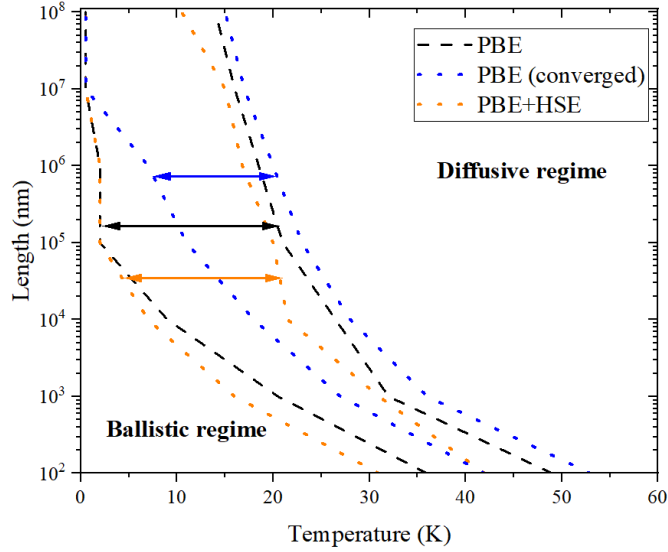


FIG. 16. Thermal transport regimes: phonon hydrodynamics regime, ballistic regime, and diffusive regime for LiF using PBE (black dashed lines), PBE (blue dots) under convergence conditions at supercell of $8 \times 8 \times 8$ (second-order), $3 \times 3 \times 3$ (third-order), and q -grid of $40 \times 40 \times 40$, and PBE with HSE (orange dots). Double arrow lines show the window of phonon hydrodynamics.

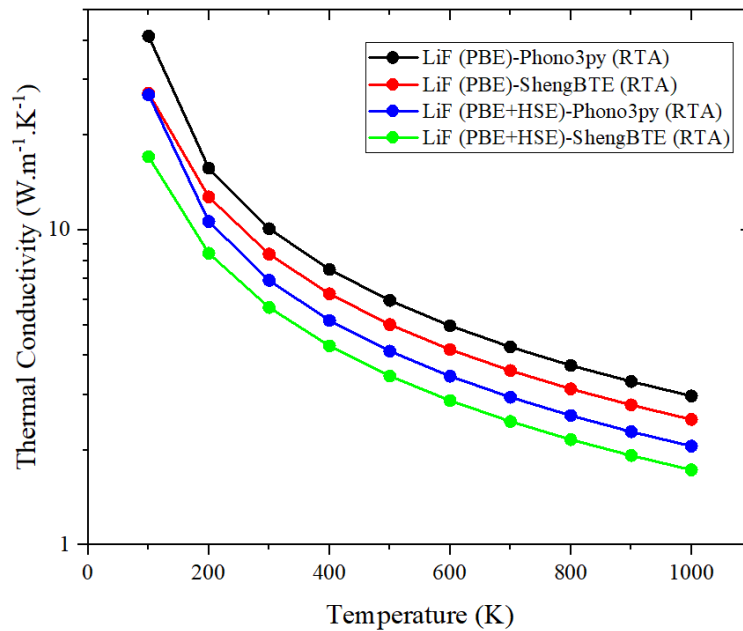


FIG. 17. Calculated lattice thermal conductivity for LiF under relaxation time approximation (RTA). Calculations were done with PBE (Phono3py: black circles, ShengBTE: red circles) and PBE with HSE (Phono3py: blue circles, ShengBTE: green circles).

One possible reason phonon calculations remain weakly, but non-negligibly impacted, by the choice of functional, thereby ensuring the reasonable accuracy of thermal calculations in contrast to electronic calculations, is the distinct impact of absolute total energies on electronic calculations and the influence of relative energy differences on phonon calculations [123]. Absolute total energies in electronic calculations suffer from inaccuracies due to the approximations made within the XC functionals. On the other hand, phonon calculations (i.e., force constants) depend on energy differences, which can be computed more reliably since any consistent error or systematic offset in energy calculations may cancel out, resulting in an accurate description of thermal properties. Even so, the influence of exchange-correlation functionals on DFT calculations is evident as demonstrated in the variability of the phonon hydrodynamics windows for all the materials studied in this work.

To summarize, Fig. 18 presents a comparison between the calculated and theoretical thermal conductivity of NaF, LiF, LiH, and NaH, at various temperatures ranging from 100 to 800 K. From this figure, it is evident that GGA functionals, on average, yield better agreement with experiments. We tested GGA with other materials, such as silicon and germanium, and found it to be the optimal functional choice in terms of structural and thermal properties. It was noted that the calculated values obtained using the PBESOL functional are generally between those obtained from the PBE and LDA functionals. In comparison with PBE, PBESOL provides structural attributes, such as lattice constant, that are more closely matched to experimental data.

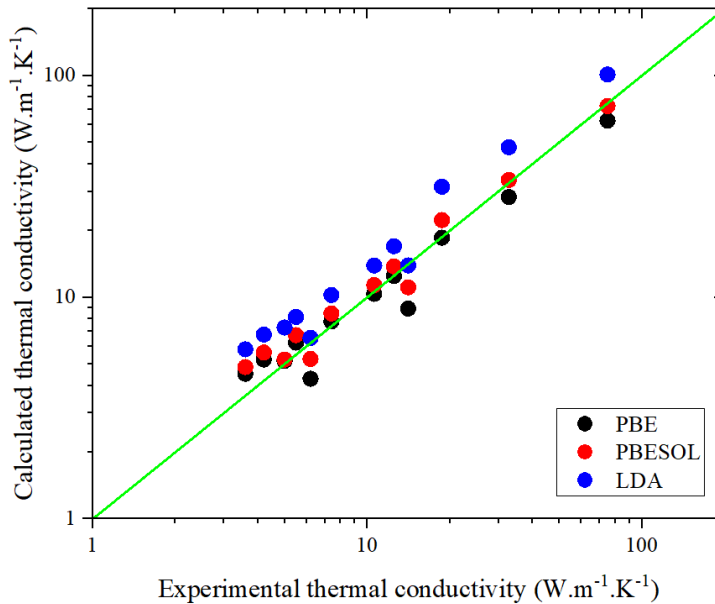


FIG. 18. Comparison between the calculated and theoretical thermal conductivity of pure NaF, LiF, LiH, and NaH. PBE (black circles), PBESOL (red circles), and LDA (blue circles). The green line indicates how closely the theoretical data aligns with the experimental findings. The nearer a point is to this line, the more it matches the experimental results.

It is important to consider the steps required to produce accurate first-principles calculations in the *absence* of experimental data. As a starting point, one can explore similar systems or elements for which functionals have been developed and validated, aiming for a close match in terms of atomic properties. In the absence of a well-established pseudopotential, one may consider generating a preliminary pseudopotential using a pseudopotential generation code, such as those based on the projector-augmented wave (PAW) method. This preliminary pseudopotential can be refined through iterative calculations, comparing the results with available experimental and theoretical data in related systems, even if indirect. Convergence of DFT input parameters, such as k-point sampling and cutoff energy, is required to remove additional sources of uncertainty. Additionally, and in the same vein as our effort to compare ShengBTE and Phonopy, beyond the selection of pseudopotential and exchange-correlation functional, there is ongoing work to benchmark the large number of available DFT codes. For instance, Bosoni *et al.* [124] proposed a protocol to enhance the reliability and precision of DFT methods and codes, providing a substantial reference dataset to foster improvements and ensure reproducibility in computational studies. The protocol leverages AiiDA workflows to streamline and ensure reproducibility in verifying DFT computations using a dataset based on all-electron methods spanning the entire periodic table [124]. To predict the error of calculations when experiments are not possible or available, uncertainty quantification may be applied [12].

V. CONCLUSIONS

Using DFT, we calculated the electrical, mechanical, and thermal properties of fluoride and alkali hydride materials using PBE, PBESOL, and LDA functionals. Phonon scattering rates were used to predict phonon hydrodynamics windows based on Guyer's condition. The impact of isotopes on lattice thermal properties and phonon hydrodynamics windows was characterized. Convergence with respect to numerical parameters was confirmed. Overall, our results demonstrated agreement with, when available, previous experimental and previous theoretical results, but non-negligible differences in the prediction of the phonon hydrodynamics due to the choice of functional were observed.

ACKNOWLEDGMENTS

This work was supported by the NSERC Discovery Grants Program under Grant No. RGPIN-2021-02957.

-
- [1] R. A. Guyer and J. A. Krumhansl, *Thermal Conductivity, Second Sound, and Phonon Hydrodynamic Phenomena in Nonmetallic Crystals*, Phys. Rev. **148**, 778 (1966).
- [2] H. E. Jackson, C. T. Walker, and T. F. McNelly, *Second Sound in NaF*, Phys. Rev. Lett. **25**, 26 (1970).
- [3] T. van Mourik, M. Bühl, and M.-P. Gaigeot, *Density Functional Theory across Chemistry, Physics and Biology*, Philos. Trans. R. Soc. A Math. Phys. Eng. Sci. **372**, 20120488 (2014).
- [4] J. P. Perdew, K. Burke, and M. Ernzerhof, *Generalized Gradient Approximation Made Simple*, Phys. Rev. Lett. **77**, 3865 (1996).
- [5] Z. Chen and J. Yang, *The B3LYP Hybrid Density Functional Study on Solids*, Front. Phys. China **1**, 339 (2006).
- [6] J. P. Perdew, A. Ruzsinszky, G. I. Csonka, O. A. Vydrov, G. E. Scuseria, L. A. Constantin, X. Zhou, and K. Burke, *Restoring the Density-Gradient Expansion for Exchange in Solids and Surfaces*, Phys. Rev. Lett. **100**, 136406 (2008).
- [7] G.-X. Zhang, A. M. Reilly, A. Tkatchenko, and M. Scheffler, *Performance of Various Density-Functional Approximations for Cohesive Properties of 64 Bulk Solids*, New J. Phys. **20**, 63020 (2018).
- [8] C. Persson and S. Mirbt, *Improved Electronic Structure and Optical Properties of Sp-Hybridized Semiconductors Using LDA+U SIC*, Brazilian J. Phys. **36**, 286 (2006).
- [9] S. Ishii, S. Iwata, and K. Ohno, *All-Electron GW Calculations of Silicon, Diamond, and Silicon Carbide*, Mater. Trans. **51**, 2150 (2010).
- [10] C.-X. Zhao, Y. Huang, J.-Q. Wang, C.-Y. Niu, and Y. Jia, *Prediction of a New Direct-Gap Silicon Phase: T36 Silicon*, Phys. Lett. A **383**, 125903 (2019).
- [11] L. Lindsay, D. A. Broido, and T. L. Reinecke, *First-Principles Determination of Ultrahigh Thermal Conductivity of Boron Arsenide: A Competitor for Diamond?*, Phys. Rev. Lett. **111**, 25901 (2013).
- [12] H. L. Parks, H.-Y. Kim, V. Viswanathan, and A. J. H. McGaughey, *Uncertainty Quantification in First-Principles Predictions of Phonon Properties and Lattice Thermal Conductivity*, Phys. Rev. Mater. **4**, 83805 (2020).
- [13] B. Mortazavi, E. V. Podryabinkin, I. S. Novikov, T. Rabczuk, X. Zhuang, and A. V. Shapeev, *Accelerating First-Principles Estimation of Thermal Conductivity by Machine-Learning Interatomic Potentials: A MTP/ShengBTE Solution*, Comput. Phys. Commun. **258**, 107583

- (2021).
- [14] A. Jain and A. J. H. McGaughey, *Effect of Exchange–correlation on First-Principles-Driven Lattice Thermal Conductivity Predictions of Crystalline Silicon*, *Comput. Mater. Sci.* **110**, 115 (2015).
 - [15] K. Ghosh, A. Kusiak, and J.-L. Battaglia, *Phonon Hydrodynamics in Crystalline GeTe at Low Temperature*, *Phys. Rev. B* **102**, 94311 (2020).
 - [16] K. Ghosh, A. Kusiak, and J.-L. Battaglia, *Phonon Hydrodynamics in Crystalline Materials*, *J. Phys. Condens. Matter* **34**, 323001 (2022).
 - [17] C. C. Ackerman and W. C. Overton, *Second Sound in Solid Helium-3*, *Phys. Rev. Lett.* **22**, 764 (1969).
 - [18] T. F. McNelly, S. J. Rogers, D. J. Channin, R. J. Rollefson, W. M. Goubau, G. E. Schmidt, J. A. Krumhansl, and R. O. Pohl, *Heat Pulses in NaF: Onset of Second Sound*, *Phys. Rev. Lett.* **24**, 100 (1970).
 - [19] V. Narayanamurti and R. C. Dynes, *Observation of Second Sound in Bismuth*, *Phys. Rev. Lett.* **28**, 1461 (1972).
 - [20] S. Huberman, R. A. Duncan, K. Chen, B. Song, V. Chiloyan, Z. Ding, A. A. Maznev, G. Chen, and K. A. Nelson, *Observation of Second Sound in Graphite at Temperatures above 100 K*, *Science (80-.)*. **364**, 375 (2019).
 - [21] Z. Ding, K. Chen, B. Song, J. Shin, A. A. Maznev, K. A. Nelson, and G. Chen, *Observation of Second Sound in Graphite over 200 K*, *Nat. Commun.* **13**, 285 (2022).
 - [22] A. Cepellotti, G. Fugallo, L. Paulatto, M. Lazzeri, F. Mauri, and N. Marzari, *Phonon Hydrodynamics in Two-Dimensional Materials*, *Nat. Commun.* **6**, 6400 (2015).
 - [23] P. D. Pathak, J. M. Trivedi, and N. G. Vasavada, *Thermal Expansion of NaF, KBr and RbBr and Temperature Variation of the Frequency Spectrum of NaF*, *Acta Crystallogr. Sect. A* **29**, 477 (1973).
 - [24] T. Liang, W.-Q. Chen, C.-E. Hu, X.-R. Chen, and Q.-F. Chen, *Lattice Dynamics and Thermal Conductivity of Lithium Fluoride via First-Principles Calculations*, *Solid State Commun.* **272**, 28 (2018).
 - [25] M. Born, K. Huang, and M. Lax, *Dynamical Theory of Crystal Lattices*, *Am. J. Phys.* **23**, 474 (1955).
 - [26] F. Tran and P. Blaha, *Accurate Band Gaps of Semiconductors and Insulators with a Semilocal Exchange-Correlation Potential*, *Phys. Rev. Lett.* **102**, 226401 (2009).
 - [27] J. A. Camargo-Martínez and R. Baquero, *Performance of the Modified Becke-Johnson Potential*

- for Semiconductors, Phys. Rev. B **86**, 195106 (2012).
- [28] I. S. Messaoudi, A. Zaoui, and M. Ferhat, *Band-Gap and Phonon Distribution in Alkali Halides*, Phys. Status Solidi **252**, 490 (2015).
- [29] H.-Y. Wang, Q.-K. Hu, C.-Y. Li, Y.-C. Wang, and G.-F. Mi, *Phase Transition, Elastic, and Thermodynamic Properties of NaF under High Pressure*, Phase Transitions **85**, 409 (2012).
- [30] S. Härtel, J. Vogt, and H. Weiss, *Relaxation and Thermal Vibrations at the NaF(100) Surface*, Surf. Sci. **604**, 1996 (2010).
- [31] M. Prencipe, A. Zupan, R. Dovesi, E. Aprà, and V. R. Saunders, *Ab Initio Study of the Structural Properties of LiF, NaF, KF, LiCl, NaCl, and KCl*, Phys. Rev. B **51**, 3391 (1995).
- [32] A. Solovyeva and O. A. von Lilienfeld, *Alchemical Screening of Ionic Crystals*, Phys. Chem. Chem. Phys. **18**, 31078 (2016).
- [33] *CRC Handbook of Chemistry and Physics* (CRC Press, 2014).
- [34] R. P. Lowndes and D. H. Martin, *Dielectric Dispersion and the Structures of Ionic Lattices*, Proc. R. Soc. London. Ser. A. Math. Phys. Sci. **308**, 473 (1969).
- [35] A. Shukla, *Ab Initio Hartree-Fock Born Effective Charges of LiH, LiF, LiCl, NaF, and NaCl*, Phys. Rev. B **61**, 13277 (2000).
- [36] G. Raunio, L. Almqvist, and R. Stedman, *Phonon Dispersion Relations in NaCl*, Phys. Rev. **178**, 1496 (1969).
- [37] F. C. Brown, C. Gähwiller, H. Fujita, A. B. Kunz, W. Scheifley, and N. Carrera, *Extreme-Ultraviolet Spectra of Ionic Crystals*, Phys. Rev. B **2**, 2126 (1970).
- [38] W. J. L. Buyers, *Lattice Dynamics of Sodium Fluoride*, Phys. Rev. **153**, 923 (1967).
- [39] J. T. Lewis, A. Lehoczky, and C. V. Briscoe, *Elastic Constants of the Alkali Halides at 4.2°K*, Phys. Rev. **161**, 877 (1967).
- [40] S. Haussühl, Z. Phys. **159**, **223**, (1960).
- [41] R. A. Miller and C. S. Smith, *Pressure Derivatives of the Elastic Constants of LiF and NaF*, J. Phys. Chem. Solids **25**, 1279 (1964).
- [42] A. Otero-de-la-Roza and V. Luaña, *Gibbs2: A New Version of the Quasi-Harmonic Model Code. I. Robust Treatment of the Static Data*, Comput. Phys. Commun. **182**, 1708 (2011).
- [43] K. Spangenberg and S. Haussühl, *Die Elastischen Konstanten Der Alkalihalogenide Vom Steinsalz-Typus*, Zeitschrift Für Krist. **109**, 422 (1957).
- [44] M. J. L. Sangster and R. M. Atwood, *Interionic Potentials for Alkali Halides. II. Completely Crystal Independent Specification of Born-Mayer Potentials*, J. Phys. C Solid State Phys. **11**,

1541 (1978).

- [45] I. A. Smirnov, *Thermal Conductivity of Sodium Fluoride Single Crystals with Potassium, Lithium, and Chlorine Impurities*, Fiz. Tverd. Tela **9**, 1845–7, (1967).
- [46] A. V Petrov, N. S. Tsyapkina, and Y. A. Logachev, *Temperature Dependence of the Thermal Conductivity of Alkali Metal Halides at Elevated Temperatures*, Fiz. Tverd. Tela **16**, 65–70, (1974).
- [47] C. T. Walker, *Thermal Conductivity of Some Alkali Halides Containing F Centers*, Phys. Rev. **132**, 1963 (1963).
- [48] A. E. Gheribi, M. Salanne, and P. Chartrand, *Formulation of Temperature-Dependent Thermal Conductivity of NaF, β -Na₃AlF₆, Na₅Al₃F₁₄, and Molten Na₃AlF₆ Supported by Equilibrium Molecular Dynamics and Density Functional Theory*, J. Phys. Chem. C **120**, 22873 (2016).
- [49] Y.S. Touloukian and E. H. Buyco, *Thermophysical Properties of Matter*, Vol. Vol.5 (1970).
- [50] C. M. Kachhava and S. C. Saxena, *Semiempirical Formulas for Thermal Expansion and Grüneisen Constants of Ionic Crystals*, J. Appl. Phys. **39**, 2973 (1968).
- [51] Y. Ekinici and J. . Toennies, *Thermal Expansion of the LiF(001) Surface*, Surf. Sci. **563**, 127 (2004).
- [52] G. Dolling, H. G. Smith, R. M. Nicklow, P. R. Vijayaraghavan, and M. K. Wilkinson, *Lattice Dynamics of Lithium Fluoride*, Phys. Rev. **168**, 970 (1968).
- [53] D. M. Roessler and W. C. Walker, *Electronic Spectrum of Crystalline Lithium Fluoride*, J. Phys. Chem. Solids **28**, 1507 (1967).
- [54] M. Piacentini, D. W. Lynch, and C. G. Olson, *Thermoreflectance of LiF between 12 and 30 eV*, Phys. Rev. B **13**, 5530 (1976).
- [55] F. J. Himpsel, L. J. Terminello, D. A. Lapiano-Smith, E. A. Eklund, and J. J. Barton, *Band Dispersion of Localized Valence States in LiF(100)*, Phys. Rev. Lett. **68**, 3611 (1992).
- [56] L. Lindsay, *Isotope Scattering and Phonon Thermal Conductivity in Light Atom Compounds: LiH and LiF*, Phys. Rev. B **94**, 174304 (2016).
- [57] H. J. Hou, H. Guan, S. R. Zhang, L. H. Xie, and L. Wang, *Structural, Phonon and Thermodynamic Properties of the Rocksalt Structure LiF from First Principles*, Mater. Sci. Forum **850**, 348 (2016).
- [58] W. G. Wyckoff, *Crystal Structures*, Wiley **Vol. 1**, (1968).
- [59] F. Bernardini and V. Fiorentini, *Electronic Dielectric Constants of Insulators Calculated by the Polarization Method*, Phys. Rev. B **58**, 15292 (1998).

- [60] M. Guo, X. Zhang, H. Gu, and N. Wang, *Ab Initio Calculations of Electronic and Optical Properties in O-Doped LiF Crystal*, *Open Phys.* **6**, (2008).
- [61] E. L. Shirley, L. J. Terminello, J. E. Klepeis, and F. J. Himpsel, *Detailed Theoretical Photoelectron Angular Distributions for LiF(100)*, *Phys. Rev. B* **53**, 10296 (1996).
- [62] A. J. Cohen and R. G. Gordon, *Theory of the Lattice Energy, Equilibrium Structure, Elastic Constants, and Pressure-Induced Phase Transitions in Alkali-Halide Crystals*, *Phys. Rev. B* **12**, 3228 (1975).
- [63] A. V. Petrov, N. S. Tsytkina, and V. E. Seleznev, *High Temp.- High. Press* **8**, **536**, (1976).
- [64] B. K. Singh, M. K. Roy, V. J. Menon, and K. C. Sood, *Effects of Dispersion, Correction Term, and Isotopes on the Thermal Conductivity of LiF Crystal*, *Phys. Rev. B* **67**, 14302 (2003).
- [65] P. D. Pathak and N. G. Vasavada, *Thermal Expansion of LiF by X-Ray Diffraction and the Temperature Variation of Its Frequency Spectrum*, *Acta Crystallogr. Sect. A* **28**, 30 (1972).
- [66] G. Simmons and H. Wang, *Single Crystal Elastic Constants and Calculated Aggregate Properties Handbook, Second Edition* (1971).
- [67] A. E. Gheribi and P. Chartrand, *Application of the CALPHAD Method to Predict the Thermal Conductivity in Dielectric and Semiconductor Crystals*, *Calphad* **39**, 70 (2012).
- [68] J. L. Verble, J. L. Warren, and J. L. Yarnell, *Lattice Dynamics of Lithium Hydride*, *Phys. Rev.* **168**, 980 (1968).
- [69] F. E. Pretzel, G. N. Rupert, C. L. Mader, E. K. Storms, G. V. Gritton, and C. C. Rushing, *Properties of Lithium Hydride I. Single Crystals*, *J. Phys. Chem. Solids* **16**, 10 (1960).
- [70] M. H. Brodsky and E. Burstein, *Infrared Lattice Vibrations of Single Crystal Lithium Hydride and Some of Its Isotopic Derivations*, *J. Phys. Chem. Solids* **28**, 1655 (1967).
- [71] G. Lucovsky, R. M. Martin, and E. Burstein, *Localized Effective Charges in Diatomic Crystals*, *Phys. Rev. B* **4**, 1367 (1971).
- [72] D. K. Blat, N. E. Zein, and V. I. Zinenko, *Calculations of Phonon Frequencies and Dielectric Constants of Alkali Hydrides via the Density Functional Method*, *J. Phys. Condens. Matter* **3**, 5515 (1991).
- [73] R. H. Lyddane, R. G. Sachs, and E. Teller, *On the Polar Vibrations of Alkali Halides*, *Phys. Rev.* **59**, 673 (1941).
- [74] D. Laplaze, *Étude Expérimentale de LiH, LiD ; Spectres de Réflexion Infrarouge et Spectres de Diffusion Raman Du Second Ordre*, *J. Phys.* **37**, 1051 (1976).
- [75] M. J. van Setten, V. A. Popa, G. A. de Wijs, and G. Brocks, *Electronic Structure and Optical*

- Properties of Lightweight Metal Hydrides*, Phys. Rev. B **75**, 35204 (2007).
- [76] X. Yang, Y. Zhao, Z. Dai, M. Zulfiqar, J. Zhu, and J. Ni, *Thermal Expansion Induced Reduction of Lattice Thermal Conductivity in Light Crystals*, Phys. Lett. A **381**, 3514 (2017).
- [77] C. E. Messer, A SURVEY REPORT ON LITHIUM HYDRIDE, 1960.
- [78] J. L. Anderson, J. Nasise, K. Phillipson, and F. E. Pretzel (deceased), *Isotopic Effects on the Thermal Expansion of Lithium Hydride*, J. Phys. Chem. Solids **31**, 613 (1970).
- [79] G. Roma, C. M. Bertoni, and S. Baroni, *The Phonon Spectra of LiH and LiD from Density-Functional Perturbation Theory*, Solid State Commun. **98**, 203 (1996).
- [80] Y. Kondo and K. Asaumi, *Effect of Pressure on the Direct Energy Gap of LiH*, J. Phys. Soc. Japan **57**, 367 (1988).
- [81] V. G. Plekhanov, *Wannier-Mott Excitons in Isotope-Disordered Crystals*, Reports Prog. Phys. **61**, 1045 (1998).
- [82] X. Yang, T. Feng, J. Li, and X. Ruan, *Stronger Role of Four-Phonon Scattering than Three-Phonon Scattering in Thermal Conductivity of III-V Semiconductors at Room Temperature*, Phys. Rev. B **100**, 245203 (2019).
- [83] L. Lindsay and D. A. Broido, *Three-Phonon Phase Space and Lattice Thermal Conductivity in Semiconductors*, J. Phys. Condens. Matter **20**, 165209 (2008).
- [84] D. G. R. William D. Callister Jr., *Fundamentals of Materials Science and Engineering* (2018).
- [85] V. G. Plekhanov, *Isotope Effects in Solid State Physics* (2001).
- [86] W. P. Mason, editor, *Physical Acoustics: Principles and Methods* (1964).
- [87] J. P. Wolfe, *Imaging Phonons* (Cambridge University Press, 1998).
- [88] J. Y. Zhang, L. J. Zhang, T. Cui, Y. L. Niu, Y. M. Ma, Z. He, and G. T. Zou, *A First-Principles Study of Electron-phonon Coupling in Electron-Doped LiH*, J. Phys. Condens. Matter **19**, 425218 (2007).
- [89] J. Hama, K. Suito, and N. Kawakami, *First-Principles Calculation of the Shock-Wave Equation of State of Isotopic Lithium Hydrides*, Phys. Rev. B **39**, 3351 (1989).
- [90] Y. Bouhadda, A. Rabehi, and S. Bezzari-Tahar-Chaouche, *First-Principle Calculation of MgH₂ and LiH for Hydrogen Storage* First-Principle Calculation of MgH₂ and LiH for Hydrogen Storage, 2007.
- [91] J. M. Besson, G. Weill, G. Hamel, R. J. Nelmes, J. S. Loveday, and S. Hull, *Equation of State of Lithium Deuteride from Neutron Diffraction under High Pressure*, Phys. Rev. B **45**, 2613 (1992).

- [92] E. Haque and A. K. M. A. Islam, *Hydrides and Deuterides of Lithium and Sodium. I. Model Potentials and Their Use in Perfect Lattice*, Phys. Status Solidi **158**, 457 (1990).
- [93] R. Pandey and A. M. Stoneham, *Intrinsic Defect Energies of Lithium Hydride and Lithium Deuteride Crystals*, J. Phys. C Solid State Phys. **18**, 5289 (1985).
- [94] W. Dyck, *Lattice Dynamics of Alkali Hydrides and Euterides with the NaCl Type Structure*, J. Phys. C Solid State Phys. **14**, 4193 (1981).
- [95] D. Gerlich and C. S. Smith, *The Pressure and Temperature Derivatives of the Elastic Moduli of Lithium Hydride*, J. Phys. Chem. Solids **35**, 1587 (1974).
- [96] J. B. Vetrano, Batelle Memorial Institute (Unpublished), Quoted by C. E. Messer and T. B. P. Gibb, Jr., 1957.
- [97] G. A. Slack, *Nonmetallic Crystals with High Thermal Conductivity*, J. Phys. Chem. Solids **34**, 321 (1973).
- [98] B. Yates, G. H. Wostenholm, and J. L. Bingham, *The Specific Heats of 7LiH and 7LiD at Low Temperatures*, J. Phys. C Solid State Phys. **7**, 1769 (1974).
- [99] A. K. M. A. Islam, E. Haque, and A. S. Azad, *Crystal Anharmonicity in Li(H,D) and Na(H,D) Systems*, Phys. Status Solidi **183**, 117 (1994).
- [100] T. D. Humphries, D. A. Sheppard, M. R. Rowles, M. V. Sofianos, and C. E. Buckley, *Fluoride Substitution in Sodium Hydride for Thermal Energy Storage Applications*, J. Mater. Chem. A **4**, 12170 (2016).
- [101] S. Bandyopadhyay, *Physics of Nanostructured Solid State Devices* (Springer US, Boston, MA, 2012).
- [102] X. Ke and I. Tanaka, *Decomposition Reactions for NaAlH₄, Na₃AlH₆, and NaH: First-Principles Study*, Phys. Rev. B **71**, 24117 (2005).
- [103] Y. Zhao, Z. Dai, C. Zhang, C. Lian, S. Zeng, G. Li, S. Meng, and J. Ni, *High Thermopower and Potential Thermoelectric Properties of Crystalline LiH and NaH*, Phys. Rev. B **95**, 14307 (2017).
- [104] X.-W. Sun, L.-C. Cai, Q.-F. Chen, X.-R. Chen, and F.-Q. Jing, *Structural, Thermodynamic, Electronic, and Optical Properties of NaH from First-Principles Calculations*, Mater. Chem. Phys. **133**, 346 (2012).
- [105] J. L. Martins, *Equations of State of Alkali Hydrides at High Pressures*, Phys. Rev. B **41**, 7883 (1990).
- [106] S. Lebègue, B. Arnaud, M. Alouani, and P. E. Blochl, *Implementation of an All-Electron GW Approximation Based on the Projector Augmented Wave Method without Plasmon Pole*

- Approximation: Application to Si, SiC, AlAs, InAs, NaH, and KH*, Phys. Rev. B **67**, 155208 (2003).
- [107] D. G. Pettifor, M. Aoki, J. N. Murrell, A. Cottrell, and A. M. Stoneham, *Bonding and Structure of Intermetallics: A New Bond Order Potential*, Philos. Trans. R. Soc. London. Ser. A Phys. Eng. Sci. **334**, 439 (1991).
- [108] S. F. Pugh, *XCII. Relations between the Elastic Moduli and the Plastic Properties of Polycrystalline Pure Metals*, London, Edinburgh, Dublin Philos. Mag. J. Sci. **45**, 823 (1954).
- [109] M. Chauhan and D. C. Gupta, *Electronic, Mechanical, Phase Transition and Thermo-Physical Properties of TiC, ZrC and HfC: High Pressure Computational Study*, Diam. Relat. Mater. **40**, 96 (2013).
- [110] A. N. Cleland, *Foundations of Nanomechanics* (Springer Berlin Heidelberg, Berlin, Heidelberg, 2003).
- [111] X.-W. Sun, Q.-F. Chen, X.-R. Chen, L.-C. Cai, and F.-Q. Jing, *Ab Initio Study of Phase Transition and Bulk Modulus of NaH*, J. Solid State Chem. **184**, 427 (2011).
- [112] J. G. O. Ojwang, R. van Santen, G. J. Kramer, A. C. T. van Duin, and W. A. Goddard, *Modeling the Sorption Dynamics of NaH Using a Reactive Force Field*, J. Chem. Phys. **128**, 164714 (2008).
- [113] S. J. Duclos, Y. K. Vohra, A. L. Ruoff, S. Filipek, and B. Baranowski, *High-Pressure Studies of NaH to 54 GPa*, Phys. Rev. B **36**, 7664 (1987).
- [114] H. D. Hochheimer, K. Strössner, W. Hönle, B. Baranowski, and F. Filipek, *High Pressure X-Ray Investigation of the Alkali Hydrides NaH, KH, RbH and CsH*, J. Less Common Met. **107**, L13 (1985).
- [115] J. E. Bird, T. D. Humphries, M. Paskevicius, L. Poupin, and C. E. Buckley, *Thermal Properties of Thermochemical Heat Storage Materials*, Phys. Chem. Chem. Phys. **22**, 4617 (2020).
- [116] W. M. Haynes et al., CRC Handbook of Chemistry and Physics Internet Version 2016 Editor-in-Chief Associate Editor, n.d.
- [117] D. R. Lide, *CRC Handbook of Chemistry and Physics: A Ready Reference Book of Chemical and Physical Data* (2004).
- [118] C. G. Shull, E. O. Wollan, G. A. Morton, and W. L. Davidson, *Neutron Diffraction Studies of NaH and NaD*, Phys. Rev. **73**, 842 (1948).
- [119] F. Tran, P. Blaha, and K. Schwarz, *Band Gap Calculations with Becke–Johnson Exchange Potential*, J. Phys. Condens. Matter **19**, 196208 (2007).
- [120] J. Heyd, G. E. Scuseria, and M. Ernzerhof, *Hybrid Functionals Based on a Screened Coulomb*

Potential, J. Chem. Phys. **118**, 8207 (2003).

- [121] A. Togo, L. Chaput, T. Tadano, and I. Tanaka, *Implementation Strategies in Phonopy and phono3py*, J. Phys. Condens. Matter **35**, 353001 (2023).
- [122] A. Togo, *First-Principles Phonon Calculations with Phonopy and Phono3py*, J. Phys. Soc. Japan **92**, (2023).
- [123] C. Carbogno et al., *Numerical Quality Control for DFT-Based Materials Databases*, Npj Comput. Mater. **8**, 69 (2022).
- [124] E. Bosoni et al., *How to Verify the Precision of Density-Functional-Theory Implementations via Reproducible and Universal Workflows*, (2023).

**SUPPLEMENTAL MATERIAL: IMPACT OF EXCHANGE-CORRELATION
FUNCTIONALS ON PHONON HYDRODYNAMICS: A STUDY OF FLUORIDES (NAF, LIF)
AND ALKALI HYDRIDES (LIH, NAH) UNDER GUYER'S CRITERIA**

I. DFT CALCULATIONS.

The DFT calculations were done using PBE, PBESOL, and LDA exchange-correlation functionals. The structures of NaF, LiF, LiH, and NaH adopt the NaCl face-centered cubic (FCC) crystal structure. For first-principles calculations, a $14 \times 14 \times 14$ κ - points mesh of Monkhorst-Pack with a convergence threshold of $1.0E-16$ Ry was chosen. Quantum ESPRESSO package [1] was used to obtain second-order interatomic force constants, whereas `thirdorder.py` [2] was used to obtain third-order interatomic force constants. BTE was solved using ShengBTE package [2]. For inputs of BTE, the supercells of harmonic force constants (second-order) and anharmonic force constants (third-order), cutoff, and q mesh are converged for each type of functional. Table I lists the supercells and q meshes that were obtained. Moreover, in Appendix B, we clarify convergence tests for lattice thermal conductivity of NaF, LiF, LiH, and NaH at room temperature to obtain an appropriate q -points mesh for BTE calculation. DFT and BTE calculations can be found at <https://github.com/jamalabouhaibeh/Calculations>

TABLE XIII. The selected supercells and q mesh for BTE.

Material	Functional	Second-order supercell	Third-order supercell	Cutoff	q mesh
NaF	PBE	$6 \times 6 \times 6$	$3 \times 3 \times 3$	-2	$30 \times 30 \times 30$
	PBESOL	$3 \times 3 \times 3$	$3 \times 3 \times 3$	-5	$35 \times 35 \times 35$
	LDA	$3 \times 3 \times 3$	$3 \times 3 \times 3$	-4	$40 \times 40 \times 40$
LiF	PBE	$8 \times 8 \times 8$	$3 \times 3 \times 3$	-2	$40 \times 40 \times 40$
	PBESOL	$6 \times 6 \times 6$	$3 \times 3 \times 3$	-2	$45 \times 45 \times 45$
	LDA	$6 \times 6 \times 6$	$3 \times 3 \times 3$	-5	$30 \times 30 \times 30$
LiH	PBE	$2 \times 2 \times 2$	$4 \times 4 \times 4$	-5	$45 \times 45 \times 45$
	PBESOL	$6 \times 6 \times 6$	$3 \times 3 \times 3$	-2	$40 \times 40 \times 40$
	LDA	$8 \times 8 \times 8$	$3 \times 3 \times 3$	-2	$35 \times 35 \times 35$
NaH	PBE	$3 \times 3 \times 3$	$4 \times 4 \times 4$	-4	$40 \times 40 \times 40$
	PBESOL	$4 \times 4 \times 4$	$3 \times 3 \times 3$	-2	$45 \times 45 \times 45$
	LDA	$8 \times 8 \times 8$	$3 \times 3 \times 3$	-2	$35 \times 35 \times 35$

II. CONVERGENCE TEST FOR LATTICE THERMAL CONDUCTIVITY VALUES.

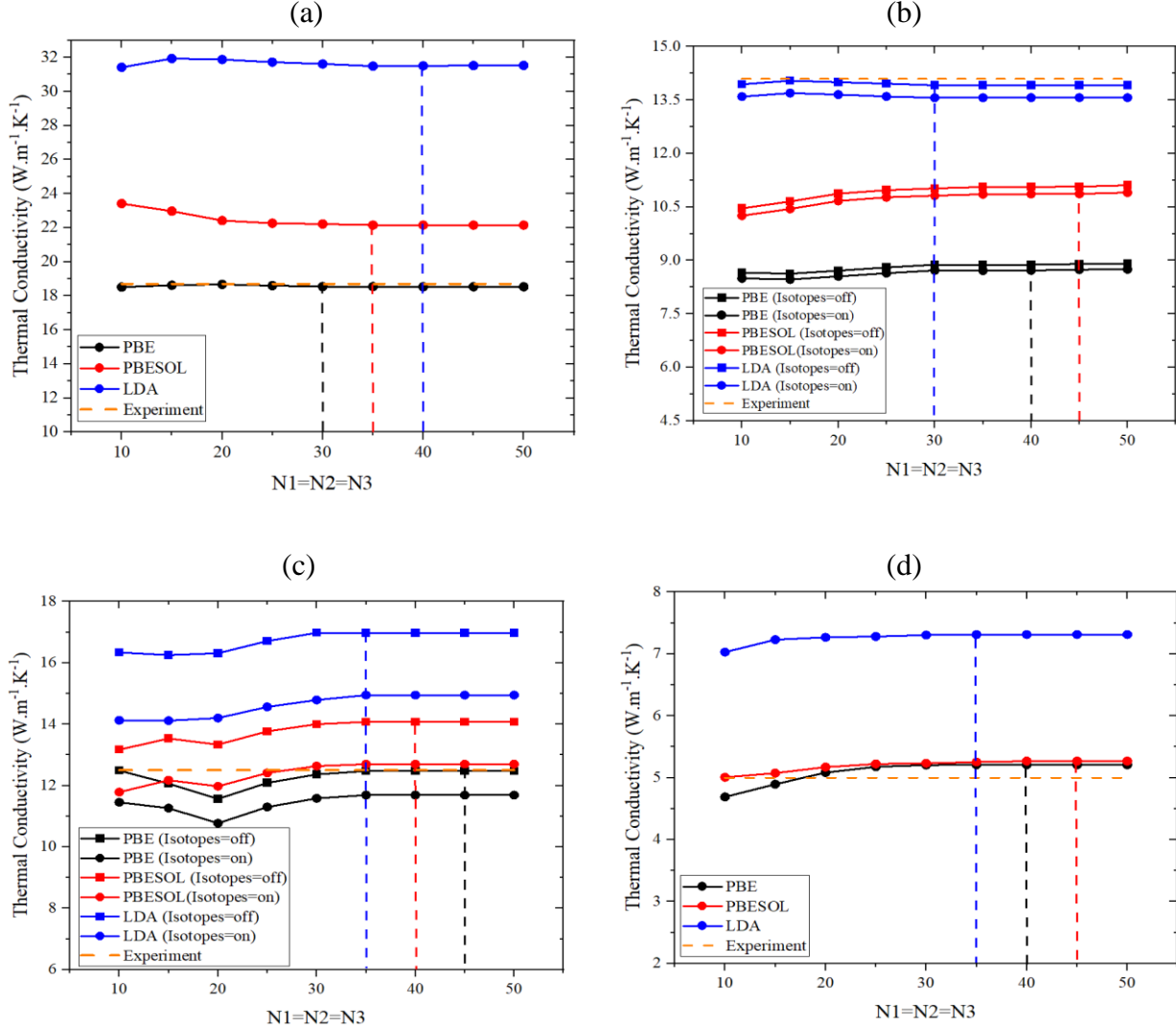


FIG. 19. Lattice thermal conductivity for different q-points numbers at room temperature for (a) NaF (b) LiF. (c) LiH. (d) NaH. The experimental values (a) [3], (b) [4], (c) [5], and (d) [6] are shown as a dashed horizontal orange line. The selected grid for each functional is shown as a dashed vertical line.

III. ELECTRICAL BAND STRUCTURES.

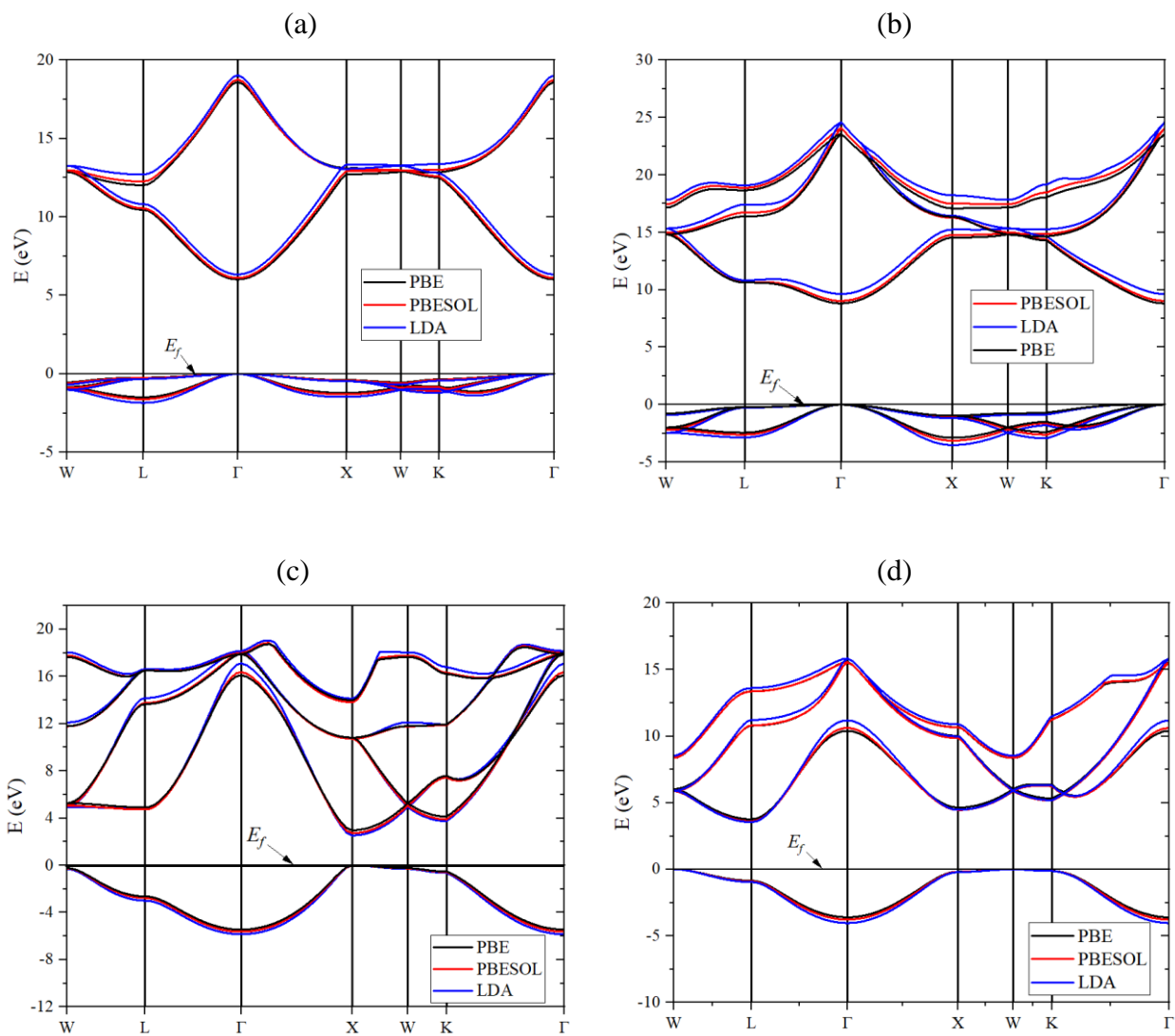


FIG. 20. Band structures of: (a) NaF. (b) LiF. (c) LiH. (d) NaH.

IV. NORMAL AND UMKLAPP SCATTERING RATES AT $T = 20$ K AND $T = 300$ K.

(1) NaF:

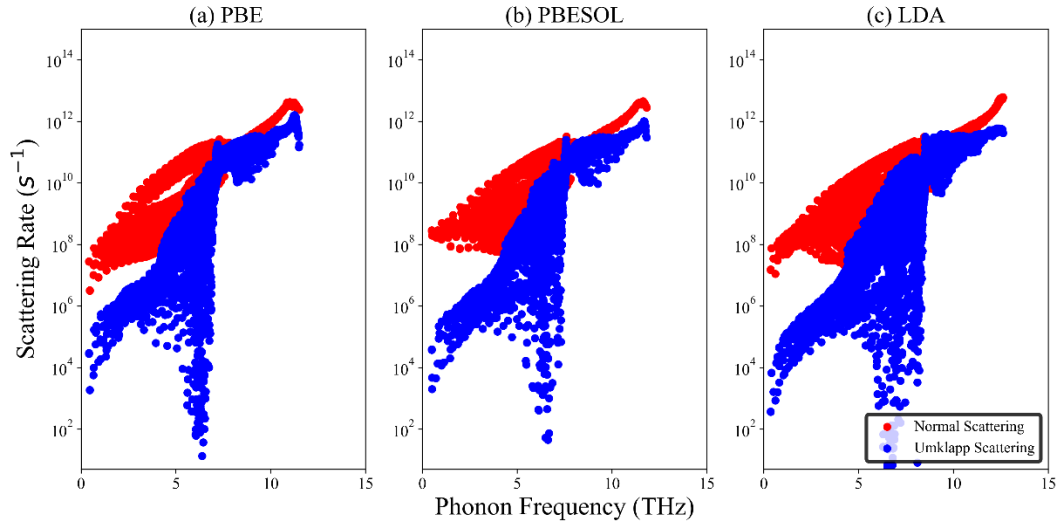


FIG. 21. Normal (red circles) and Umklapp (blue circles) scattering rates for NaF at $T = 20$ K. (a) PBE. (b) PBESOL. (c) LDA.

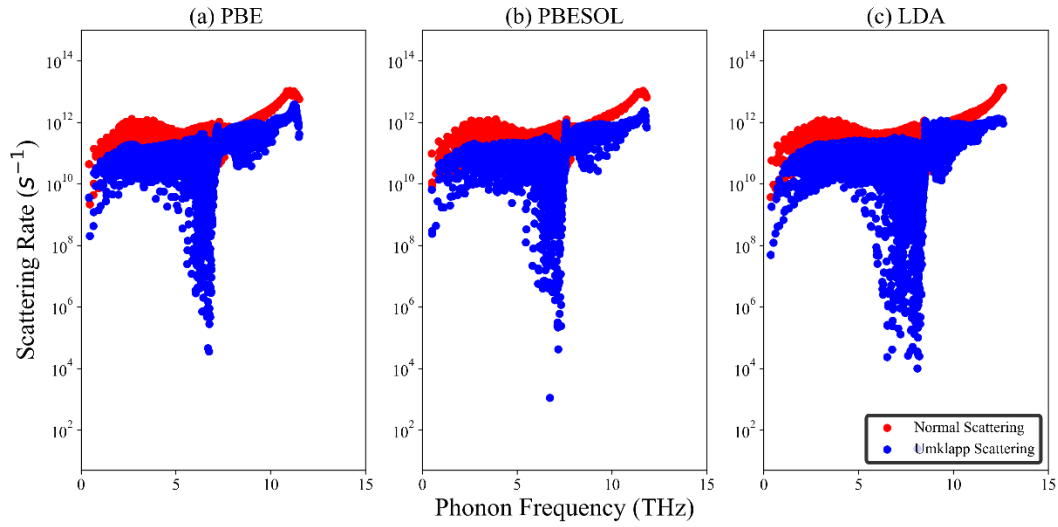


FIG. 22. Normal (red circles) and Umklapp (blue circles) scattering rates for NaF at $T = 300$ K. (a) PBE. (b) PBESOL. (c) LDA.

(2) LiF:

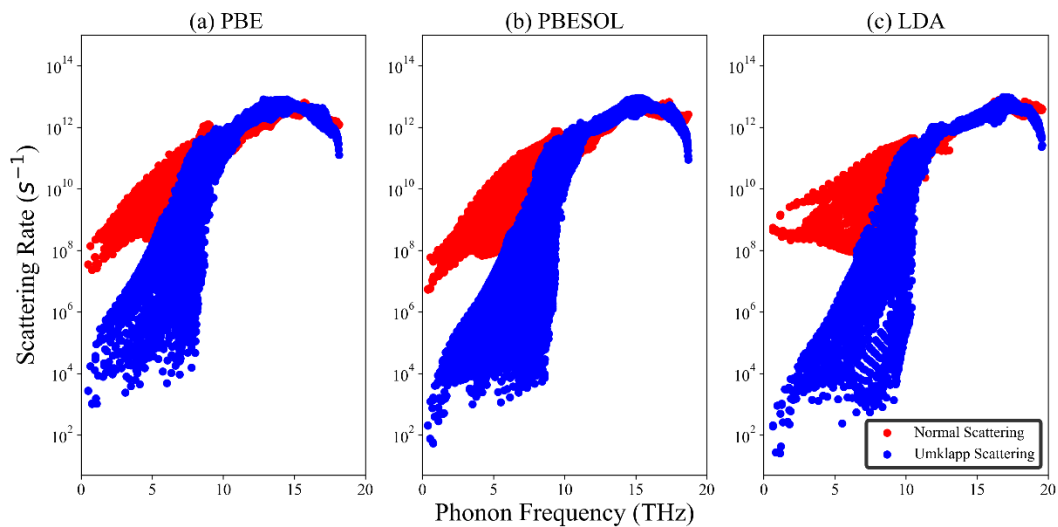


FIG. 23. Normal (red circles) and Umklapp (blue circles) scattering rates for LiF at $T = 20$ K. (a) PBE. (b) PBESOL. (c) LDA.

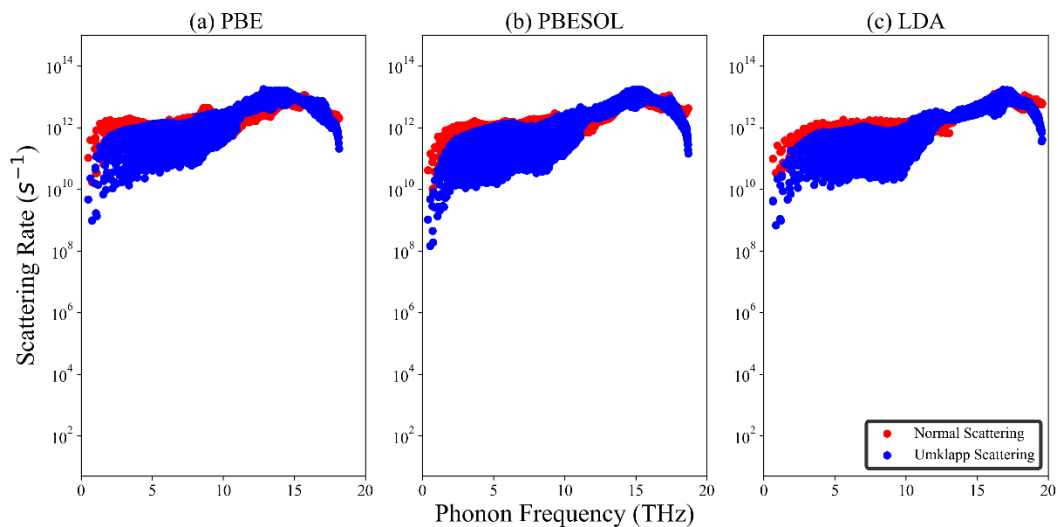


FIG. 24. Normal (red circles) and Umklapp (blue circles) scattering rates for LiF at $T = 300$ K. (a) PBE. (b) PBESOL. (c) LDA.

(3) LiH:

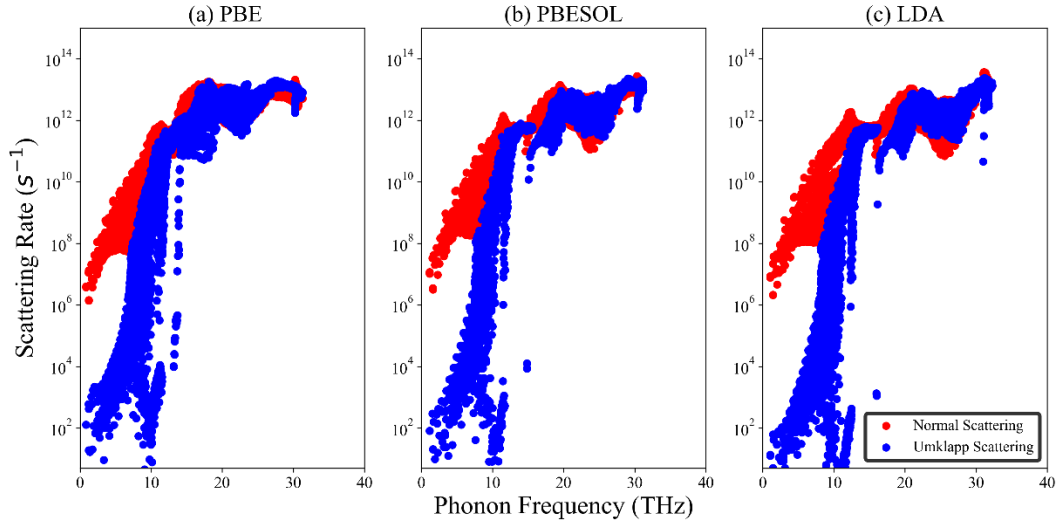


FIG. 25. Normal (red circles) and Umklapp (blue circles) scattering rates for LiH at $T = 20$ K. (a) PBE. (b) PBESOL. (c) LDA.

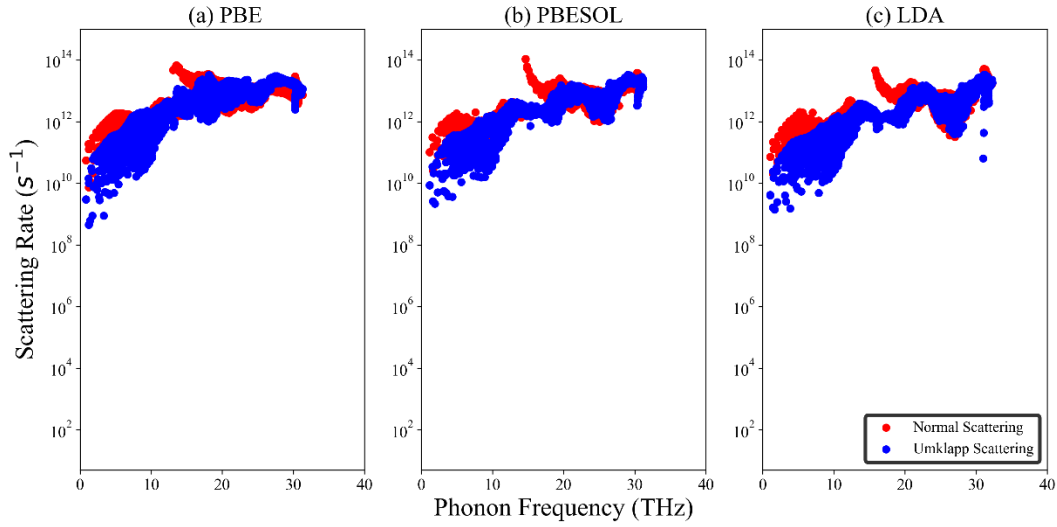


FIG. 26. Normal (red circles) and Umklapp (blue circles) scattering rates for LiH at $T = 300$ K. (a) PBE. (b) PBESOL. (c) LDA.

(4) NaH:

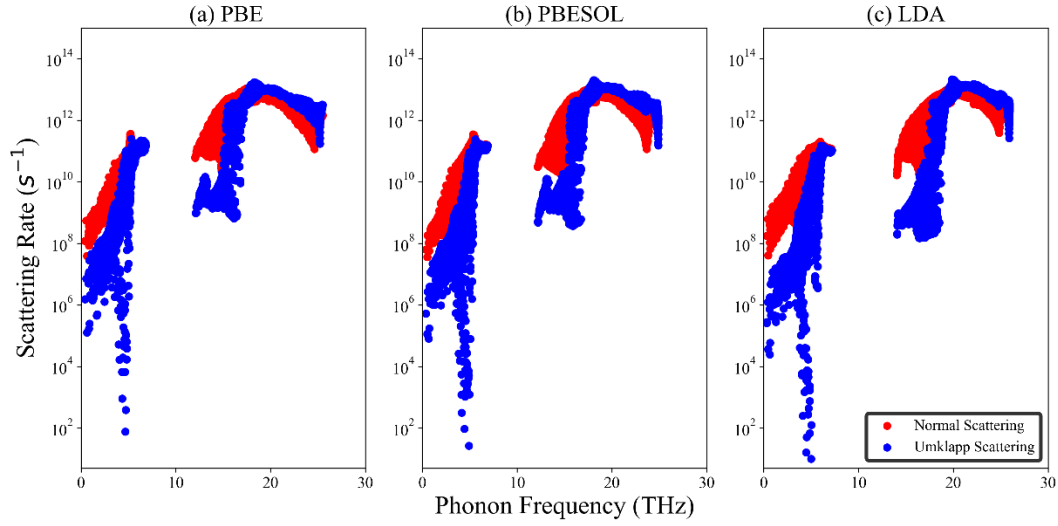


FIG. 27. Normal (red circles) and Umklapp (blue circles) scattering rates for NaH at $T = 20$ K. (a) PBE. (b) PBESOL. (c) LDA.

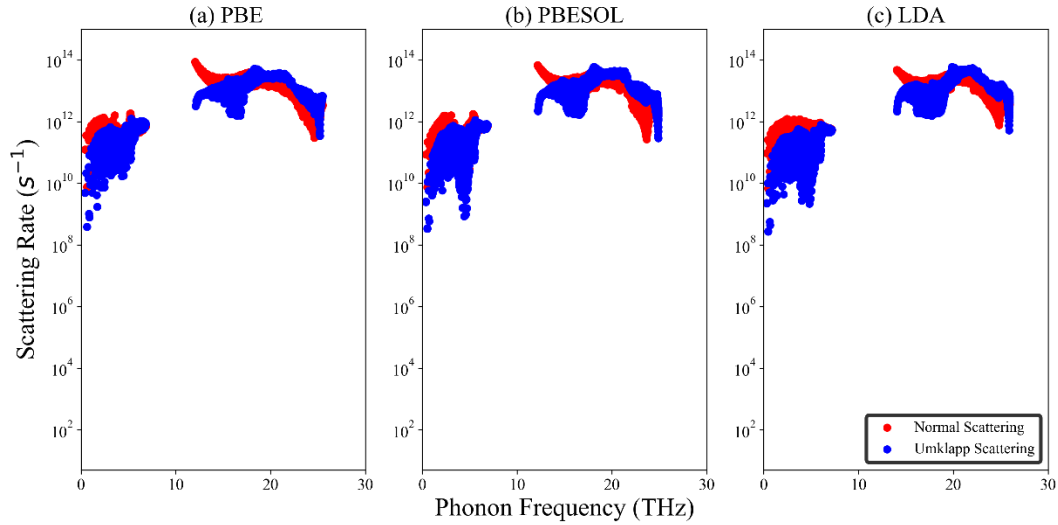


FIG. 28. Normal (red circles) and Umklapp (blue circles) scattering rates for NaH at $T = 300$ K. (a) PBE. (b) PBESOL. (c) LDA.

V. PHONON HYDRODYNAMICS WINDOWS FOR PURE CRYSTALS.

(1) NaF:

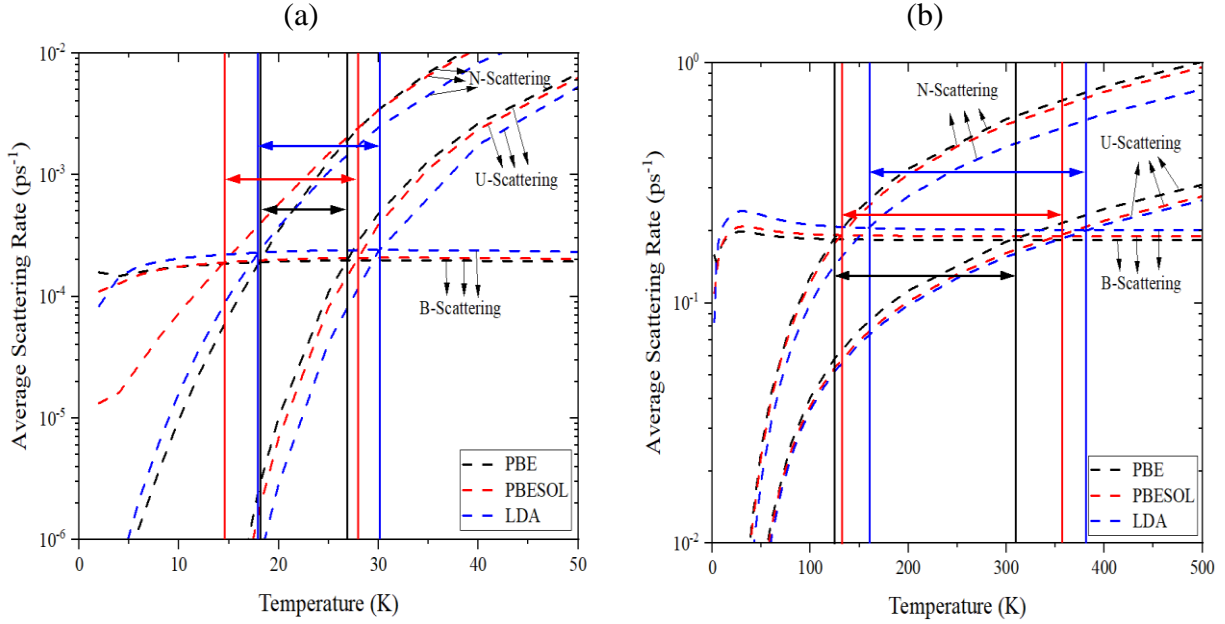


FIG. 29. Phonon hydrodynamics windows for NaF. Calculations were done with PBE (black dashed lines), PBESOL (red dashed lines), and LDA (blue dashed lines). Double arrow lines show the window of phonon hydrodynamics for each functional. (a) At $L = 10 \mu\text{m}$. (b) At $L = 10 \text{ nm}$.

(2) LiF:

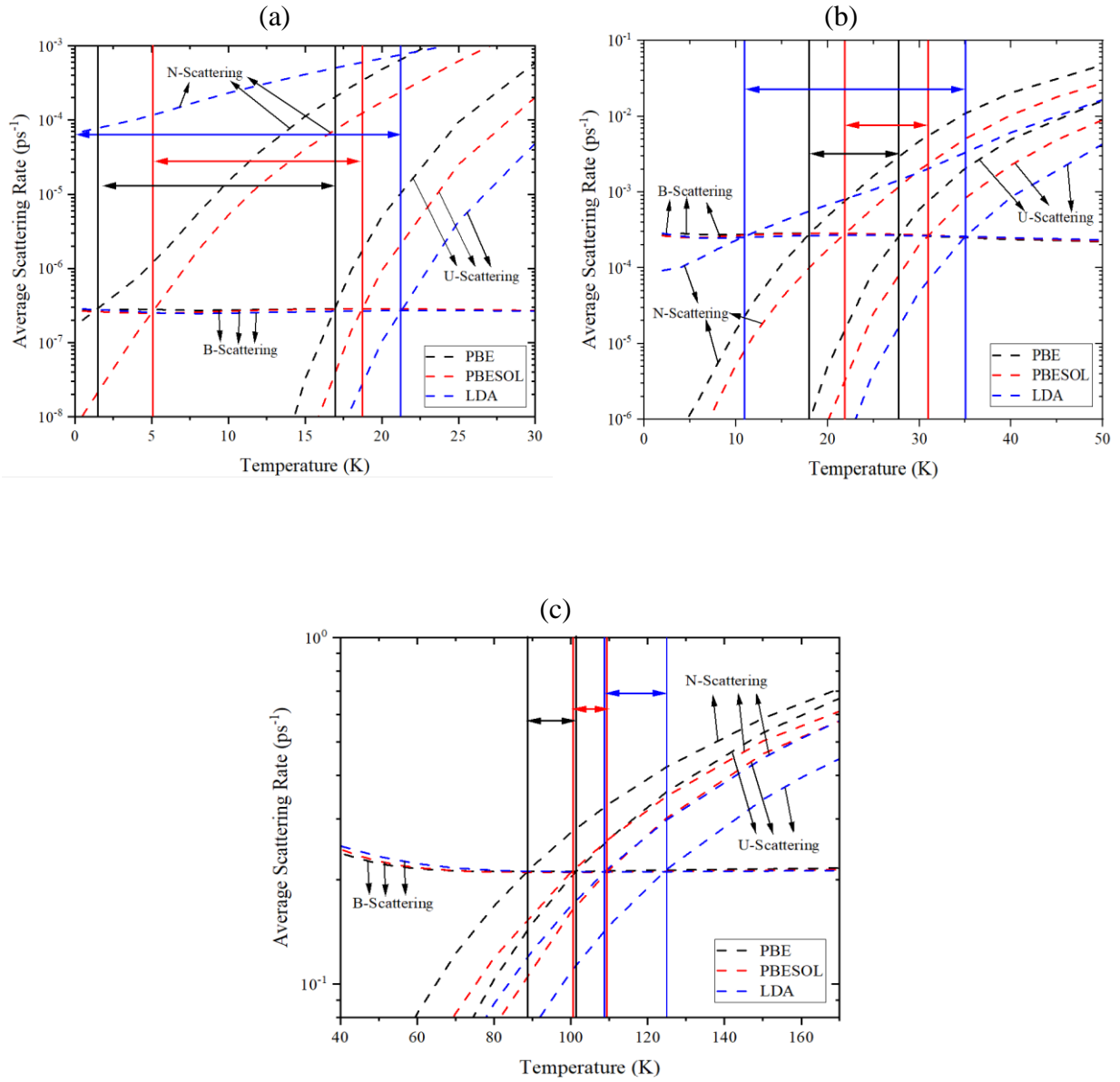


FIG. 30. Phonon hydrodynamics windows for LiF. Calculations were done with PBE (black dashed lines), PBESOL (red dashed lines), and LDA (blue dashed lines). Double arrow lines show the window of phonon hydrodynamics for each functional. (a) At $L = 10$ mm. (b) At $L = 10$ μ m. (c) At $L = 10$ nm.

(3) LiH:

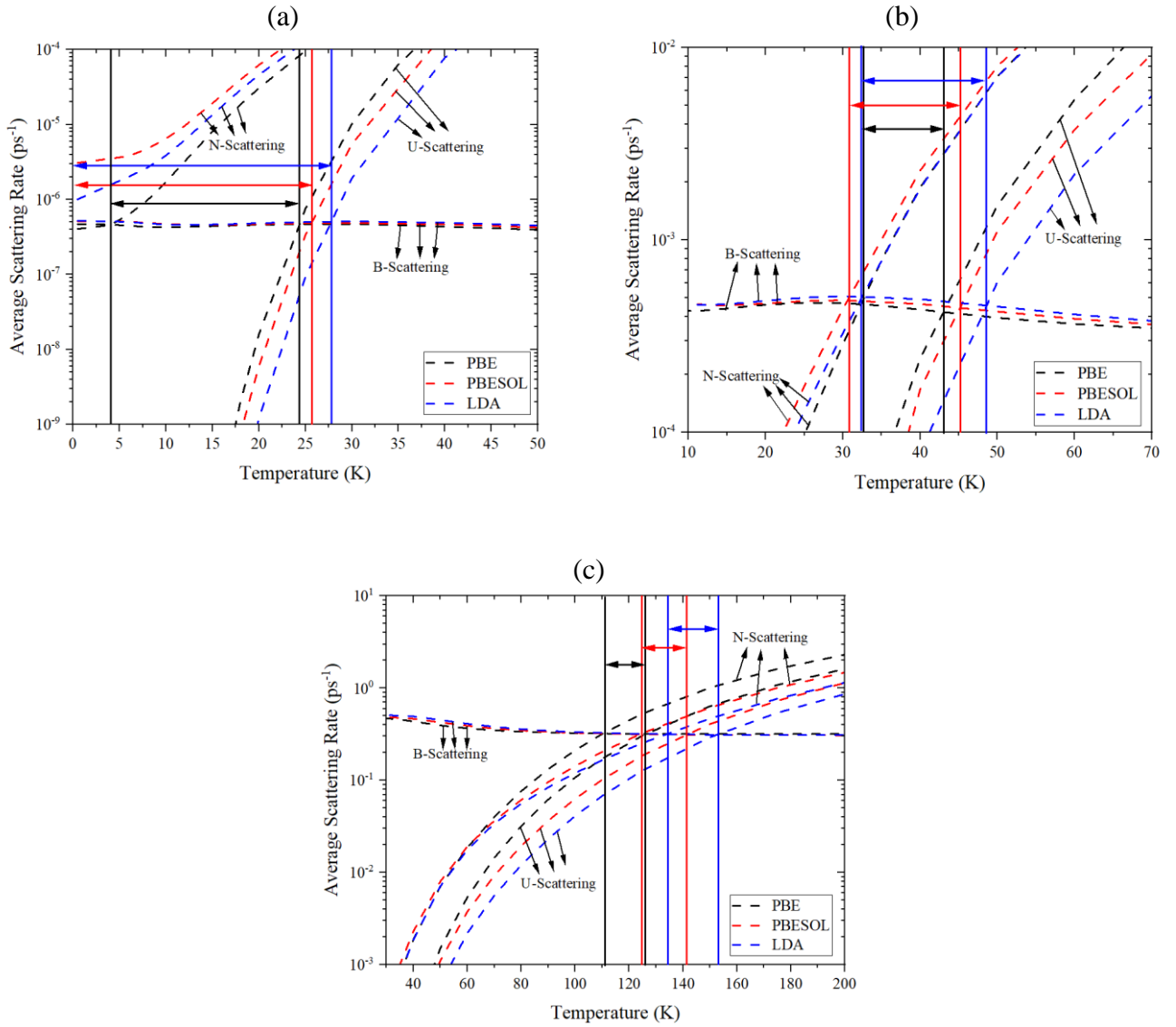


FIG. 31. Phonon hydrodynamics windows for LiH. Calculations were done with PBE (black dashed lines), PBESOL (red dashed lines), and LDA (blue dashed lines). Double arrow lines show the window of phonon hydrodynamics for each functional. (a) At $L = 10$ mm. (b) At $L = 10$ μ m. (c) At $L = 10$ nm.

(4) NaH:

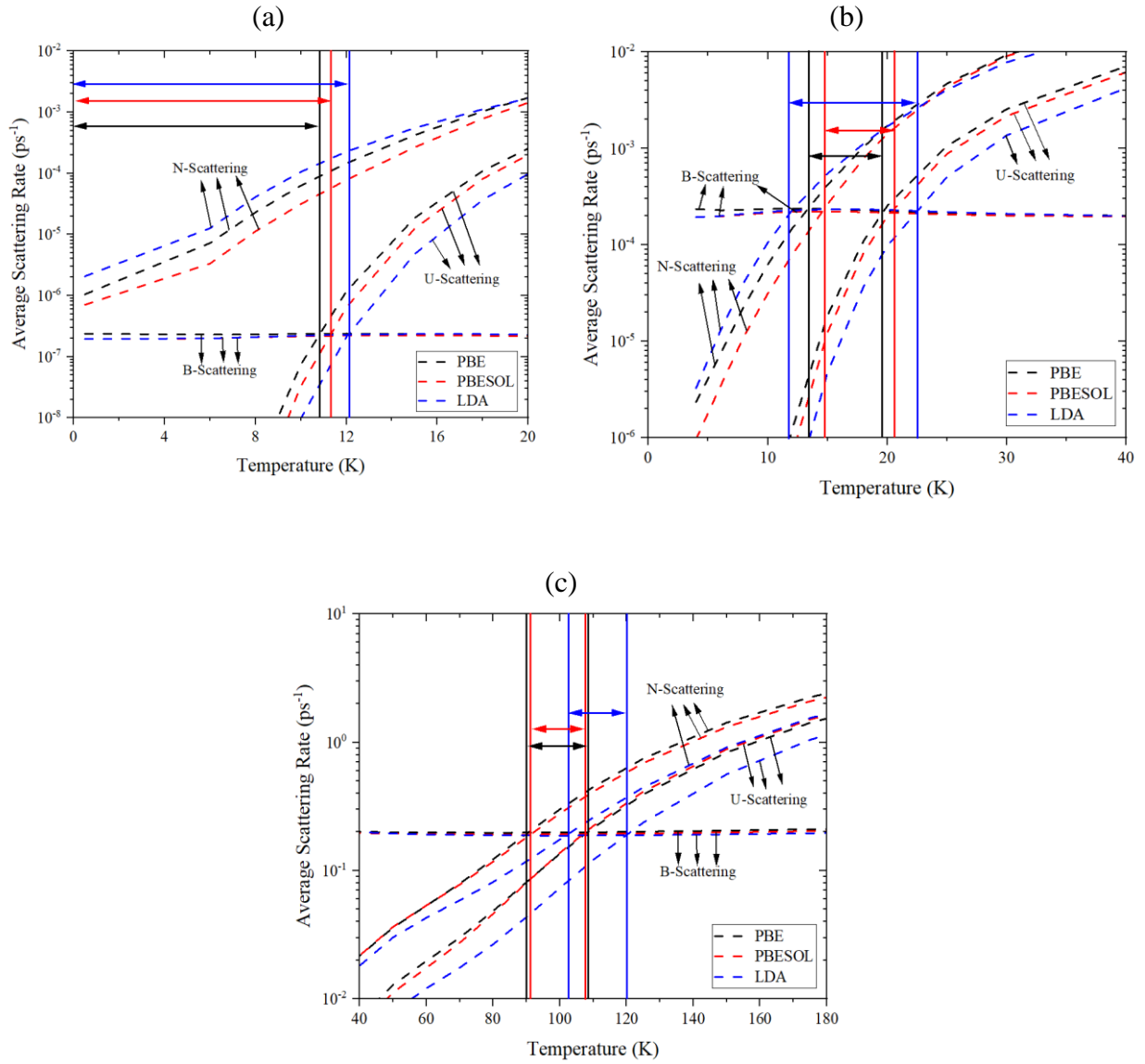
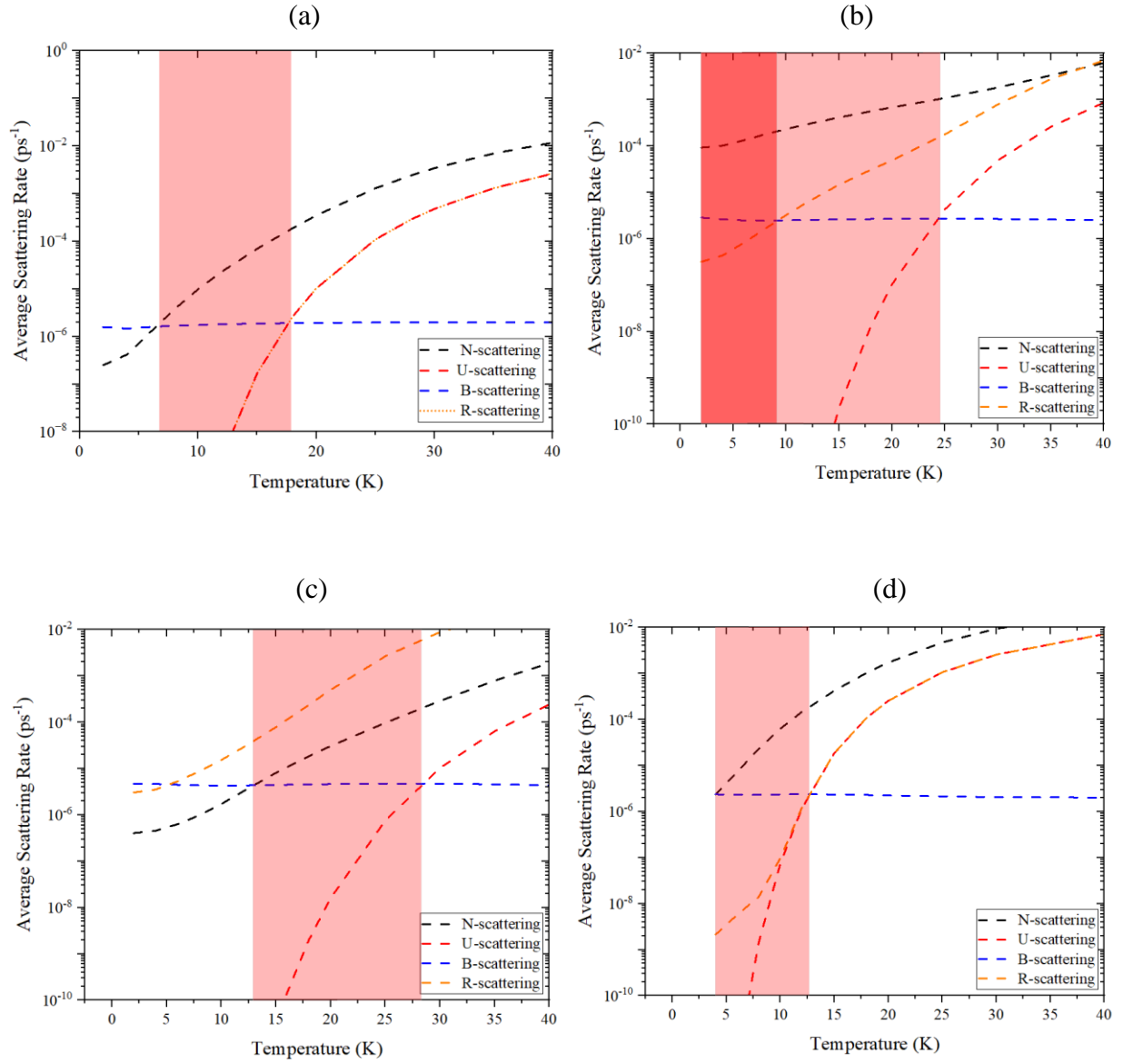


FIG. 32. Phonon hydrodynamics windows for NaH. Calculations were done with PBE (black dashed lines), PBESOL (red dashed lines), and LDA (blue dashed lines). Double arrow lines show the window of phonon hydrodynamics for each functional. (a) At $L = 10$ mm. (b) At $L = 10$ μ m. (c) At $L = 10$ nm.

VI. PHONON HYDRODYNAMICS WINDOWS INCLUDING ISOTOPE SCATTERING.



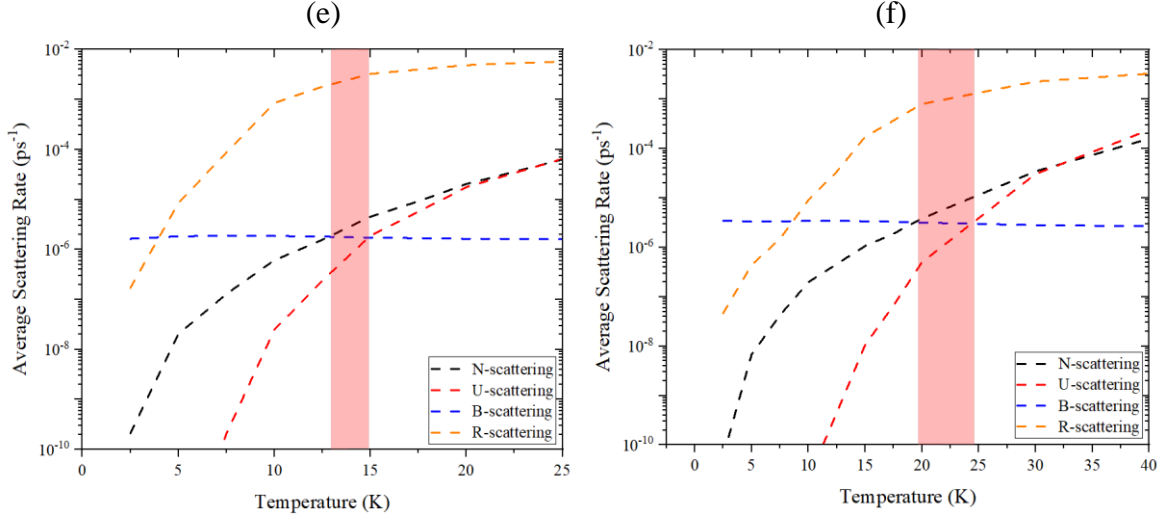


FIG. 33. Phonon hydrodynamics windows for pure materials (shaded transparent red region) and with impurity (shaded red region) at $L = 1$ mm for: (a) NaF using PBE. (b) LiF using LDA. (c) LiH using PBE. (d) NaH using PBE. (e) Ge (adapted from Ref. [7]). (f) Si. The scattering rates are denoted by colors: N-scattering (black dashed lines), U-scattering (red dashed lines), B-scattering (blue dashed lines), and R-scattering (orange dashed lines).

VII. THERMAL TRANSPORT REGIMES INCLUDING ISOTOPE SCATTERING.

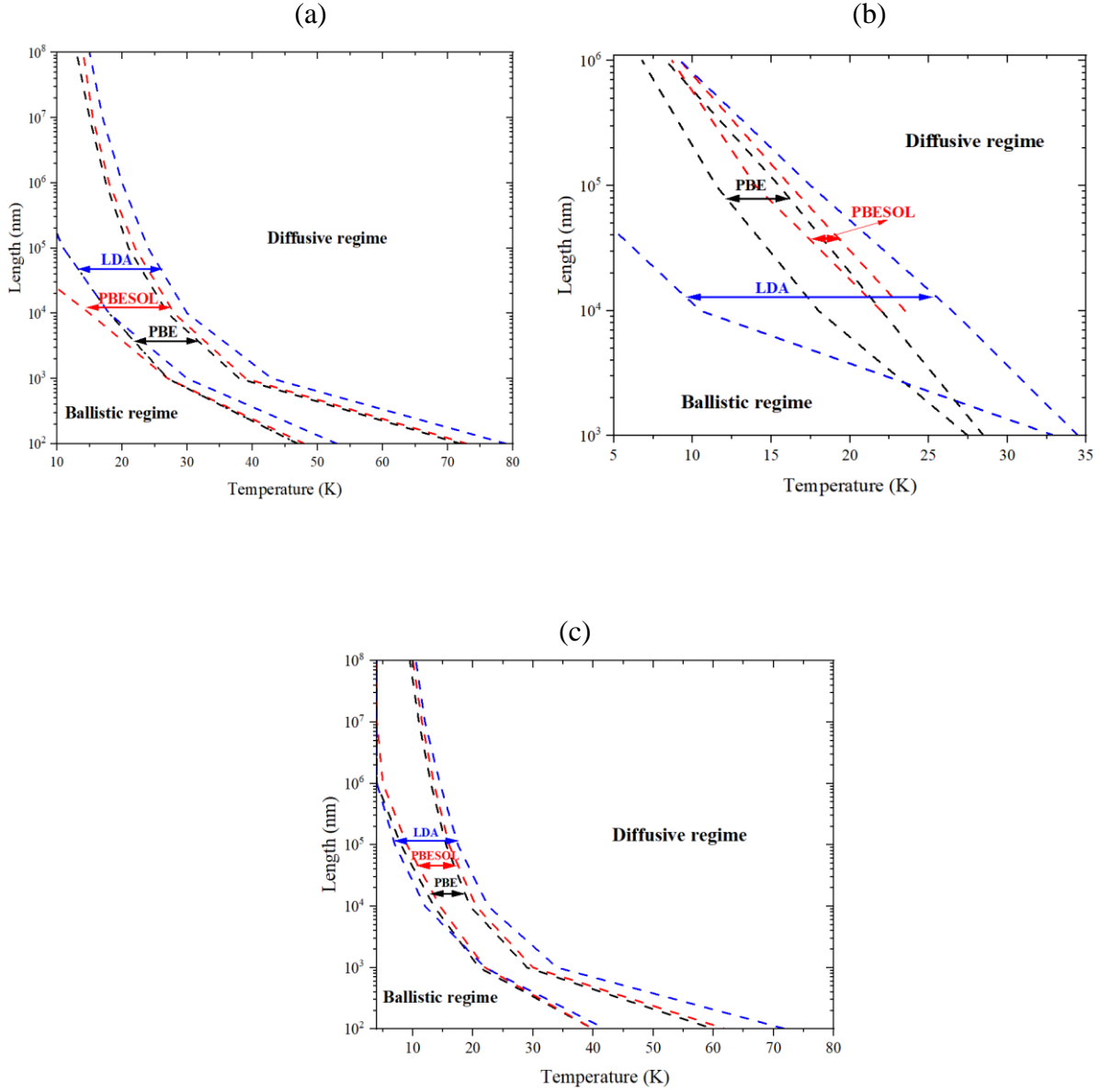


FIG. 34. Thermal transport regimes: hydrodynamics regime, ballistic regime, and diffusive regime for (a) NaF, (b) LiF, and (c) NaH. Double arrow lines show the window of phonon hydrodynamics for each functional.

- [1] P. Giannozzi et al., *QUANTUM ESPRESSO: A Modular and Open-Source Software Project for Quantum Simulations of Materials*, J. Phys. Condens. Matter **21**, 395502 (2009).
- [2] W. Li, J. Carrete, N. A. Katcho, and N. Mingo, *ShengBTE: A Solver of the Boltzmann Transport Equation for Phonons*, Comput. Phys. Commun. **185**, 1747 (2014).
- [3] I. A. Smirnov, *Thermal Conductivity of Sodium Fluoride Single Crystals with Potassium, Lithium, and Chlorine Impurities*, Fiz. Tverd. Tela **9**, 1845–7, (1967).
- [4] A. V. Petrov, N. S. Tsypkina, and V. E. Seleznev, High Temp.- High. Press **8**, 536, (1976).
- [5] J. B. Vetrano, Battelle Memorial Institute (Unpublished), Quoted by C. E. Messer and T. B. P. Gibb, Jr., 1957.
- [6] J. E. Bird, T. D. Humphries, M. Paskevicius, L. Poupin, and C. E. Buckley, *Thermal Properties of Thermochemical Heat Storage Materials*, Phys. Chem. Chem. Phys. **22**, 4617 (2020).
- [7] S. Huberman, C. Zhang, and J. Abou Haibeh, *On the Question of Second Sound in Germanium: A Theoretical Viewpoint*, (2022).